

Maternal-Fetal Immune Responses in Pregnant Women Infected with SARS-CoV-2

Valeria Garcia-Flores

Wayne State University

Roberto Romero

Wayne State University <https://orcid.org/0000-0002-4448-5121>

Yi Xu

Wayne State University

Kevin Theis

Wayne State University

Marcia Arenas-Hernandez

Wayne State University

Derek Miller

Wayne State University <https://orcid.org/0000-0002-5812-7771>

Azam Peyvandipour

Wayne State University

Jose Galaz

Wayne State University

Dustyn Levenson

Wayne State University

Gaurav Bhatti

Perinatology Research Branch

Meyer Gershater

Wayne State University

Errile Pusod

Wayne State University

David Kracht

Wayne State University

Violetta Florova

Wayne State University

Yaozhu Leng

Wayne State University

Li Tao

Wayne State University

Megan Faucett

Wayne State University

Robert Para

Wayne State University

Chaur-Dong Hsu

Wayne State University

Gary Zhang

Wayne State University

Adi Tarca

Wayne State University <https://orcid.org/0000-0003-1712-7588>

Roger Pique-Regi

Wayne State University

Nardhy Gomez-Lopez (✉ ngomezlo@med.wayne.edu)

Wayne State University <https://orcid.org/0000-0002-3406-5262>

Article

Keywords: Cytokines, COVID-19, Fetus, Immunoglobulins, IgG, IgM, Macrophages, Neonatal Immunity, Placenta, T cells, Umbilical Cord

Posted Date: March 31st, 2021

DOI: <https://doi.org/10.21203/rs.3.rs-362886/v1>

License:  This work is licensed under a Creative Commons Attribution 4.0 International License.

[Read Full License](#)

Version of Record: A version of this preprint was published at Nature Communications on January 18th, 2022. See the published version at <https://doi.org/10.1038/s41467-021-27745-z>.

1 **Maternal-Fetal Immune Responses in Pregnant Women Infected with SARS-CoV-2**

2 Valeria Garcia-Flores^{1,2}, Roberto Romero^{1,3-7,*}, Yi Xu^{1,2}, Kevin Theis^{1,2,8}, Marcia Arenas-

3 Hernandez^{1,2}, Derek Miller^{1,2}, Azam Peyvandipour^{1,2,5}, Jose Galaz^{1,2}, Dustyn Levenson^{1,2},

4 Gaurav Bhatti^{1,2}, Meyer Gershater^{1,2}, Errile Pusod^{1,2}, David Kracht^{1,2}, Violetta Florova^{1,2},

5 Yaozhu Leng^{1,2}, Li Tao^{1,2}, Megan Faucett^{1,2}, Robert Para^{1,2}, Chaur-Dong Hsu^{1,2,9}, Gary Zhang⁵,

6 Adi L. Tarca^{1,2,10}, Roger Pique-Regi^{1,2,5,*}, Nardhy Gomez-Lopez^{1,2,8,11,*}

7
8 ¹Perinatology Research Branch, Division of Obstetrics and Maternal-Fetal Medicine, Division of

9 Intramural Research, *Eunice Kennedy Shriver* National Institute of Child Health and Human

10 Development, National Institutes of Health, U.S. Department of Health and Human Services

11 (NICHD/NIH/DHHS); Bethesda, Maryland, 20892 and Detroit, Michigan, 48201, USA;

12 ²Department of Obstetrics and Gynecology, Wayne State University School of Medicine,

13 Detroit, Michigan, 48201, USA;

14 ³Department of Obstetrics and Gynecology, University of Michigan, Ann Arbor, Michigan,

15 48109, USA;

16 ⁴Department of Epidemiology and Biostatistics, Michigan State University, East Lansing,

17 Michigan, 48824, USA;

18 ⁵Center for Molecular Medicine and Genetics, Wayne State University, Detroit, Michigan,

19 48201, USA;

20 ⁶Detroit Medical Center, Detroit, Michigan, 48201, USA;

21 ⁷Department of Obstetrics and Gynecology, Florida International University, Miami, Florida,

22 33199, USA;

23 ⁸Department of Biochemistry, Microbiology and Immunology, Wayne State University School
24 of Medicine, Detroit, Michigan, 48201, USA;

25 ⁹Department of Physiology, Wayne State University School of Medicine, Detroit, Michigan
26 48201, USA;

27 ¹⁰Department of Computer Science, Wayne State University College of Engineering, Detroit,
28 Michigan, 48201, USA

29 ¹¹Lead contact

30 *Correspondence:

31 nardhy.gomez-lopez@wayne.edu

32 rpique@wayne.edu

33 prbchiefstaff@med.wayne.edu

34

35 **ABSTRACT**

36 Pregnant women are a high-risk population for severe/critical COVID-19 and mortality.
37 However, the maternal-fetal immune responses initiated by SARS-CoV-2 infection, and whether
38 this virus is detectable in the placenta, are still under investigation. Herein, we report that SARS-
39 CoV-2 infection during pregnancy primarily induced specific maternal inflammatory responses
40 in the circulation and at the maternal-fetal interface, the latter being governed by T cells and
41 macrophages. SARS-CoV-2 infection during pregnancy was also associated with a cytokine
42 response in the fetal circulation (i.e. umbilical cord blood) without compromising the cellular
43 immune repertoire. Moreover, SARS-CoV-2 infection neither altered fetal cellular immune
44 responses in the placenta nor induced elevated cord blood levels of IgM. Importantly, SARS-
45 CoV-2 was not detected in the placental tissues, nor was the sterility of the placenta
46 compromised by maternal viral infection. This study provides insight into the maternal-fetal
47 immune responses triggered by SARS-CoV-2 and further emphasizes the rarity of placental
48 infection.

49

50 **KEYWORDS:** Cytokines, COVID-19, Fetus, Immunoglobulins, IgG, IgM, Macrophages,
51 Neonatal Immunity, Placenta, T cells, Umbilical Cord

52

53 **INTRODUCTION**

54 To date, over 65,000 pregnant women in the United States have been infected with
55 SARS-CoV-2¹, the virus responsible for the coronavirus disease 2019 (COVID-19). During
56 pregnancy, SARS-CoV-2 infection can lead to variable outcomes, which range from
57 experiencing no symptoms to developing severe/critical disease^{2,3}. Most pregnant women with
58 SARS-CoV-2 infection are asymptomatic or only experience mild symptoms^{4,5}. Regardless, in
59 the first six months of the COVID-19 pandemic, it was documented that pregnant women with
60 SARS-CoV-2 were at an increased risk for hospitalization, mechanical ventilation, intensive care
61 unit admission, and preterm birth^{2,3,6-8}, but rates of maternal mortality were reported to be similar
62 between pregnant and non-pregnant women⁶. More recently, it has been clearly shown that
63 pregnant women are at a high risk for severe/critical disease and mortality as well as preterm
64 birth⁹⁻¹². Therefore, investigating host immune responses in pregnant women infected with
65 SARS-CoV-2, even if they are asymptomatic, is timely.

66 Most neonates born to infected women test negative for SARS-CoV-2, and the majority
67 of those testing positive for the virus present symptoms that are not severe^{8,13}. For the latter
68 group, the timing of mother-to-child transmission (i.e. vertical transmission) of SARS-CoV-2 is
69 still unclear, since this can occur *in utero*, intrapartum, or early in the postnatal period¹⁴. Yet,
70 while rare¹⁴, there is already evidence of SARS-CoV-2 *in utero* vertical transmission^{15,16}, which
71 is likely to occur through the hematogenous route (i.e. bloodstream infection)¹⁷. In such cases,
72 the virus must cross the maternal-fetal interface by infecting the syncytiotrophoblast layer of the
73 placenta to gain access to the fetal circulation. The mechanisms whereby SARS-CoV-2 infects
74 placental cells are still under investigation; however, it is well accepted that coronaviruses can
75 enter host cells via two main canonical mechanisms^{18,19}: 1) the direct pathway, in which host

76 cells are required to express both the angiotensin-converting enzyme 2 (ACE-2) receptor²⁰ and
77 the serine protease TMPRSS2²¹; and 2) the endosomal route, in which cell entry can be mediated
78 by ACE-2 alone. Using both single-cell and single-nuclear RNA sequencing, we have previously
79 shown that the co-expression of ACE-2 and TMPRSS2 is negligible in first, second, and third
80 trimester placental cells²². Subsequent investigations demonstrated that the ACE-2 protein was
81 polarized to the stromal (fetal) side of the syncytiotrophoblast and TMPRSS2 limited to the
82 villous endothelium^{23,24}. Yet, placental cells can express non-canonical cell entry mediators such
83 as cathepsin L (CSTL), FURIN, and SIGLEC1, among others²². Furthermore, SARS-CoV-2
84 infection can be associated with vascular damage in pregnant women, in whom ischemic injury
85 of the placenta may facilitate viral cell entry²⁵. Therefore, SARS-CoV-2 can infect placental
86 cells, as has already been reported²⁶⁻²⁸; however, placental infection alone is not considered
87 confirmatory evidence of *in utero* vertical transmission¹⁴. Nonetheless, it is possible that the
88 maternal inflammatory response induced by SARS-CoV-2 infection has deleterious effects on
89 the offspring. Therefore, investigating the host immune response in the umbilical cord blood as
90 well as at the site of maternal-fetal interactions (i.e. the maternal-fetal interface) may shed light
91 on the adverse effects of SARS-CoV-2 infection during pregnancy.

92 In the current study, we undertook a multidisciplinary approach that included the
93 detection of SARS-CoV-2 IgM/IgG, multiplex cytokine assays, immunophenotyping, single-cell
94 transcriptomics, and viral RNA and protein detection, together with the assessment of the
95 microbiome diversity and histopathology of the placenta, to characterize the maternal-fetal
96 immune responses triggered by SARS-CoV-2 during pregnancy.

97

98 **RESULTS**

99 **Characteristics of the study population**

100 A total of 15 pregnant women were enrolled in our study. The demographic and clinical
101 characteristics of the study population are displayed in Supplementary Table 1. Maternal blood
102 samples were collected upon admission, prior to administration of any medication. Seven
103 pregnant women tested RT-PCR positive (nasopharyngeal swab) for SARS-CoV-2; five were
104 asymptomatic, one had mild symptoms (e.g. fever, tachycardia), and one was diagnosed as
105 having severe COVID-19 (requiring oxygen supplementation). SARS-CoV-2 positive and
106 control non-infected women all delivered term neonates. Neonates were not RT-qPCR tested for
107 SARS-CoV-2; thus, infection status throughout the manuscript refers solely to the mother. No
108 differences in demographic and clinical characteristics were found between the study groups,
109 including Apgar scores and placental histopathological lesions.

110

111 **Pregnant women with SARS-CoV-2 infection and their neonates exhibit distinct IgM**
112 **responses**

113 Previous studies have shown that maternal IgG antibodies are transferred across the
114 placenta in both symptomatic and asymptomatic women infected with SARS-CoV-2²⁹. In
115 addition, there is evidence showing that neonates born to mothers with COVID-19 can have
116 detectable SARS-CoV-2 IgM as well as IgG^{16,30}. The presence of IgG is likely due to the passive
117 transfer of this immunoglobulin from the mother to the fetus across the placenta. However,
118 detectable levels of IgM suggest that the fetus was infected with SARS-CoV-2, given that this
119 immunoglobulin cannot cross the placenta due to its large molecular weight. Therefore, we first
120 determined the concentrations of SARS-CoV-2-specific IgM and IgG in the maternal and
121 umbilical cord blood (hereafter referred to as ‘cord blood’). As expected, pregnant women with

122 SARS-CoV-2 infection had higher levels of IgM and IgG than controls (Fig. 1A). The IgM and
123 IgG serum levels of the pregnant woman with severe COVID-19 were similar to those without
124 symptoms or with mild symptoms. In addition, IgG was increased in the cord blood of neonates
125 born to women infected with SARS-CoV-2 infection but IgM was undetected, similar to control
126 neonates (Fig. 1A). Therefore, serological data imply that in our study population, which is
127 largely asymptomatic for COVID-19, none of the neonates seems to be infected with SARS-
128 CoV-2.

129

130 **Pro-inflammatory cytokine responses are displayed in the circulation of pregnant women** 131 **with SARS-CoV-2 infection and their neonates**

132 The pathophysiology of SARS-CoV-2 infection includes a cytokine storm in the systemic
133 circulation, which can lead to multi-organ damage^{31,32}. Hence, we next determined the systemic
134 cytokine response in mothers and neonates by measuring the concentrations of 20 cytokines in
135 maternal and cord blood plasma. Pregnant women infected with SARS-CoV-2 had increased
136 systemic concentrations of IL-15 (0.43-log₂ fold change) and tended to have higher
137 concentrations of IFN- γ (1.84-log₂ fold change) and IL-8 (1.25-log₂ fold change) compared to
138 control mothers; yet, these increments did not reach statistical significance (Fig. 1B,
139 Supplementary Fig. 1, Supplementary Table 2). Such changes were not driven by the severe
140 COVID-19 case. Neonates born to women infected with SARS-CoV-2 had increased
141 concentrations of IL-17A (1.61-log₂ fold change) and TNF (1.01-log₂ fold change), but lower
142 concentrations of IL-6 (-2.90-log₂ fold change), compared to those born to control mothers (Fig.
143 1C). In addition, neonates born to women who tested positive for SARS-CoV-2 tended to display
144 higher concentrations of several cytokines including IL-12/IL-23p40 (1.32-log₂ fold change),

145 VEGF (1.56-log₂ fold change), IL-5 (1.23-log₂ fold change), and IL-8 (0.99-log₂ fold change)
146 than those born to control mothers (Fig. 1C, Supplementary Fig. 2, Supplementary Table 2).
147 Such inflammatory changes in the neonates were not solely driven by the severe COVID-19
148 case. Based on an unsupervised analysis, the primary source of variability in the maternal and
149 fetal cytokine responses was the SARS-CoV-2 infection status (first principal components in Fig.
150 1D&E significant between groups, $p < 0.05$ for both). These results show that a cytokine response
151 is observed in both the maternal and fetal circulation upon maternal infection with SARS-CoV-2.

152

153 **Pregnant women with SARS-CoV-2 infection, but not their neonates, undergo a T-cell** 154 **reduction in the circulation**

155 Previous studies have shown that patients with moderate or severe COVID-19 display
156 alterations in their cellular immune responses in the peripheral circulation³²⁻³⁴. Therefore, we
157 investigated whether pregnant women with SARS-CoV-2 infection and their neonates had
158 changes in their cellular immune repertoire using immunophenotyping (Fig. 2A, Supplementary
159 Fig. 3A). Immunophenotyping included the identification of general leukocyte subpopulations as
160 well as monocyte, neutrophil, B-cell, and T-cell subsets. Neutrophil and monocyte function has
161 also been implicated in the pathogenesis of SARS-CoV-2 infection³⁴⁻³⁶; therefore, reactive
162 oxygen species (ROS) production by neutrophils and monocytes was also determined in maternal
163 and cord blood (Supplementary Fig. 4A). No statistical differences were observed in the total
164 number of general leukocyte subpopulations or in the monocyte, neutrophil, activated T-cell, and
165 B-cell subsets (Supplementary Fig. 3B-F). Although neutrophils and monocytes produced ROS
166 when stimulated, no differences were found between SARS-CoV-2 cases and controls in the
167 maternal blood or in the cord blood (Supplementary Fig. 4B&C). Nonetheless, pregnant women

168 with SARS-CoV-2 infection had reduced T-cell numbers, but their neonates did not display such
169 a decline (Fig. 2B). Heatmap and principal component analysis (PCA) representations of the
170 immunophenotyping of the maternal blood showed that SARS-CoV-2 infection mildly altered T-
171 cell subsets (Fig. 2C&D). Specifically, pregnant women infected with SARS-CoV-2 had reduced
172 numbers of CD4⁺ T cells, including T_{CM} and Th1-like cells, as well as CD8⁺ T cells, including
173 T_{CM}, T_{EM}, and Tc17-like cells (Fig. 3A&B). Such changes were not solely driven by the severe
174 COVID-19 case. Neonates born to women with SARS-CoV-2 infection did not display changes
175 in the T-cell subsets that were affected in mothers (Fig. 3C). These data showed that pregnant
176 women infected with SARS-CoV-2 undergo a reduction in T-cell subsets, including pro-
177 inflammatory Th1- and Tc17-like cells, which is not translated to the neonatal T-cell repertoire.
178

179 **Single-cell RNA sequencing reveals perturbed maternal T-cell and macrophage responses** 180 **at the maternal-fetal interface of women with SARS-CoV-2 infection**

181 Next, we investigated whether SARS-CoV-2 infection in the mother could alter cellular
182 immune responses in the placenta, the organ that serves as the lungs, gut, kidneys, and liver of
183 the fetus^{37,38}. We performed single-cell RNA sequencing (scRNAseq) of the placental tissues
184 including the basal plate (placental villous and basal plate, PVBP) and the chorioamniotic
185 membranes (CAM) from pregnant women with SARS-CoV-2 infection and controls, using
186 established methods. Consistent with our previous studies^{22,39}, multiple cell clusters were
187 identified in the placental tissues including lymphoid and myeloid immune cells, trophoblast cell
188 types, stromal cells, and endometrial/decidual cells as well as endothelial cells (Fig. 4A).
189 Differences in abundance among cell type clusters were observed between placental
190 compartments as well as between tissues from women with SARS-CoV-2 infection and those

191 from controls (Fig. 4B&C). Further analysis revealed that the majority of the differentially
192 expressed genes (DEGs, Supplementary Table 3) between SARS-CoV-2 positive cases and
193 controls belong to immune cells from the CAM, namely maternal T cells and macrophages (Fig.
194 4D&E). Lymphatic endothelial decidual (LED) cells of maternal origin displayed three DEGs
195 between SARS-CoV-2 cases and controls. In general, fetal cell types were minimally altered by
196 the presence of SARS-CoV-2 infection in the mother (Fig. 4D&E).

197 The effects of SARS-CoV-2 on gene expression in maternal T cells from the CAM and
198 PVBP were compared to those from peripheral T cells from hospitalized COVID-19 patients⁴⁰,
199 which we will refer to as the reference database hereafter. Maternal T-cell gene expression
200 changes resulting from SARS-CoV-2 infection in the CAMs were positively correlated with
201 those in the reference database (T cells from patients with COVID-19) (Spearman's $\rho = 0.40$, $p =$
202 0.0002 ; Fig. 5A), suggesting a significant degree of shared DEGs. Yet, maternal T-cell gene
203 expression induced by SARS-CoV-2 in the CAM was also distinct, since 21 out of the 31
204 identified DEGs were not found in the reference database. In contrast, maternal T-cell gene
205 expression dysregulation in the PVBP was not correlated with that from the reference database
206 (Spearman's ρ not significantly different from 0, $p = 0.75$; Fig. 5A). Enrichment analysis
207 revealed that the shared DEGs between maternal T cells in the CAMs and the reference T-cell
208 data included translational termination and elongation, mitochondrial translational termination
209 and elongation, and regulation of TGF β receptor signaling (Supplementary Fig. 5A&B).

210 Although most of the DEGs were detected in the maternal T cells in the CAM, maternal
211 macrophages and other cell types such as maternal monocytes, maternal LED, fetal trophoblast
212 cell types, and fetal stromal cells also contributed to the differential gene expression observed
213 between SARS-CoV-2 cases and controls (Fig. 5B). The top upregulated and downregulated

214 genes in maternal T cells and macrophages are also displayed in Fig. 5C showing that changes in
215 gene expression were not always homogeneous across all the cells (e.g., *FARSA* in T cells, and
216 *TRAF5* in macrophages). Gene set enrichment analysis of the DEGs in maternal T cells and
217 macrophages type 1 using Gene Ontology (GO) terms revealed that mitochondrial translational
218 processes as well as defense response to virus and angiogenesis are processes enriched in the
219 placental tissues from mothers infected with SARS-CoV-2 (Fig. 5D). Over-representation
220 analysis using the DEGs in maternal macrophage type 2 revealed significant KEGG pathways
221 including the NOD-like receptor signaling pathway and cytokine-cytokine receptor interactions
222 (Fig. 5E). Lastly, STRING enrichment analysis of all DEGs in the CAM and PVBP showed that
223 the interactions between GO terms including cytosol, DNA replication factor A complex,
224 ESCRT III complex, I-kappa B/NF-kappaB complex, proteasome core complex, and alpha-
225 subunit complex are enriched in the placental tissues of women with SARS-CoV-2 infection
226 (Supplementary Fig. 6A).

227 Taken together, these data show that placentas from women with SARS-CoV-2 display
228 alterations in their immune repertoire, mainly in maternal T cells and macrophages infiltrating
229 the gestational tissues surrounding the fetus during gestation. Yet, the effect of SARS-CoV-2 in
230 the fetal immune cell types is minimal in our largely asymptomatic population.

231

232 **SARS-CoV-2 RNA and proteins are not detected in the placentas of infected women**

233 SARS-CoV-2 induced altered maternal T cell and macrophage responses in the CAM;
234 therefore, we explored whether this virus was present in the placental tissues. First, using a
235 scRNAseq approach, Viral-Track⁴¹, we explored whether viral sequences were detected in the
236 scRNAseq data of CAMs and PVBP from women with SARS-CoV-2 infection. SARS-CoV-2

237 viral sequences were detected in positive controls (bronchoalveolar lavage of patients infected
238 with SARS-CoV-2⁴¹) but not in the placental tissues from women with SARS-CoV-2 infection
239 (Supplementary Fig. 6B&C).

240 Subsequently, we investigated the presence of viral RNA in the CAM, basal plate (BP),
241 and placental villi (PV) using RT-qPCR for the N1 and N2 viral genes (Supplementary Fig. 7A).
242 SARS-CoV-2 N1 and N2 proteins were not detected in any of the placental samples from women
243 with SARS-CoV-2 infection or healthy controls (Supplementary Fig. 7B). Yet, in the spike-in
244 positive control, N1 and N2 RNA was detected in the CAM, BP, and PV. A sensitivity assay
245 revealed that 10 is the minimum confident copy number of viral particles detectable in the
246 placental villi using RT-qPCR (Supplementary Fig. 7C).

247 Next, we determined whether the spike and nucleocapsid proteins were detected in the
248 placental tissues of women with SARS-CoV-2 infection using immunohistochemistry (Fig. 6A).
249 Several histological slides from the CAM, BP, and PV were included in our evaluation,
250 including negative and spike-in positive controls (Supplementary Table 4). Both SARS-CoV-2
251 spike and nucleocapsid proteins were identified in the spike-in positive controls in the CAM, PB,
252 and BP (Fig. 6B). A few of the placentas from asymptomatic women with SARS-CoV-2
253 infection displayed a putative positive signal for the spike and nucleocapsid proteins (Fig. 6C);
254 yet, in all other cases, the placental tissues were negative for the SARS-CoV-2 proteins (Fig.
255 6D). As expected, spike and nucleocapsid SARS-CoV-2 proteins were not detected in the
256 placental tissues of control women (Fig. 6E). To verify the detection of SARS-CoV-2 in the
257 placental tissues, RNA was isolated from the same FFPE tissue sections where the putative
258 positive signals were observed and RT-qPCR for the N1 and N2 viral genes was performed.
259 FFPE tissue sections from the placental tissues of control women and spike-in positive controls

260 were also included. None of the placentas from women with SARS-CoV-2 infection or controls
261 had detectable levels of N1 and N2 RNA viral genes; yet, the spike-in positive controls were
262 detected (Fig. 6F).

263 Collectively, these data show that SARS-CoV-2 is not detected in the placental tissues,
264 including the chorioamniotic membranes, of women infected with SARS-CoV-2.

265

266 **SARS-CoV-2 infection during pregnancy does not compromise the sterility of the placenta**

267 Lastly, we investigated whether SARS-CoV-2 infection during pregnancy affected the
268 molecular microbial profiles of the placental tissues, including the chorioamniotic membranes.
269 Specifically, we used 16S rRNA gene qPCR and sequencing to characterize the bacterial DNA
270 load and profiles of the amnion-chorion interface of the extraplacental chorioamniotic
271 membranes, the amnion-chorion interface of the placental disc, and the placental villous tree
272 (Fig. 7A). Mode of delivery was the principal factor affecting bacterial DNA load
273 (Supplementary Table 5) and profile. Very few samples (4/15) from cesarean deliveries had a
274 bacterial DNA load exceeding that of technical controls for background DNA contamination (i.e.
275 blank DNA extraction kits), yet almost all of the samples (29/30) from vaginal deliveries did
276 (Fig. 7B). Furthermore, whereas the bacterial DNA profiles of samples from cesarean deliveries
277 were similar to those of technical controls, those from vaginal deliveries were distinct, being
278 dominated by DNA signals from *Lactobacillus* and *Ureaplasma*, similar to the vaginal swab
279 positive controls (Fig. 7C). Among the samples obtained from vaginal deliveries, there was no
280 difference in the bacterial DNA profiles based on maternal SARS-CoV-2 infection status (Fig.
281 7D). These findings show that, although mode of delivery alters the bacterial DNA loads and

282 profiles of the placental tissues, we did not find evidence that the same is true for maternal
283 SARS-CoV-2 infection.

284 **DISCUSSION**

285 This study provides evidence that, in a largely asymptomatic population, SARS-CoV-2
286 infection in pregnancy is primarily associated with maternal inflammatory responses in the
287 circulation and at the maternal-fetal interface. First, we showed that pregnant women with
288 SARS-CoV-2 infection had elevated levels of IgM and IgG in the peripheral circulation, whereas
289 only IgG was detectable in the cord blood of their neonates, suggesting that acute fetal infection
290 did not occur. This finding is consistent with several reports showing that IgM is undetected in
291 the cord blood of neonates born to women with SARS-CoV-2 infection^{29,42,43}. However, few
292 studies have demonstrated that both IgM and IgG are detectable in a small fraction of neonates
293 born to women diagnosed with COVID-19^{16,24,30}. The increased levels of IgG in the cord blood
294 are explained by the fact that this immunoglobulin crosses the placenta via the neonatal Fc
295 receptor (nFcR), which is highly expressed in the syncytiotrophoblast layer^{44,45}. Yet, it has been
296 recently reported that, in the third trimester, the mechanisms whereby SARS-CoV-2-specific
297 IgG1 crosses the placenta are compromised due to altered glycosylation profiles⁴⁶. In contrast,
298 IgM cannot cross the placenta due to its large molecular weight, and thus the detection of this
299 immunoglobulin in the cord blood represents an acute fetal response in the clinical setting^{47,48}.
300 Therefore, the absence of detectable IgM in the cord blood suggests that vertical transmission *in*
301 *utero* of SARS-CoV-2 was unlikely to occur in our study population.

302 In the current study, we report that pregnant women mount a mild systemic inflammatory
303 response to SARS-CoV-2, which is consistent with observations in asymptomatic non-pregnant
304 individuals with SARS-CoV-2 infection⁴⁹. Interestingly, we found that neonates born to SARS-
305 CoV-2-infected mothers also demonstrated increased levels of cytokines such as IL-17A and
306 TNF in the cord blood. IL-17A is a pro-inflammatory cytokine associated with a hyper-

307 inflammatory state and severe immunopathologies⁵⁰, including COVID-19⁵¹. Indeed, the severity
308 of COVID-19 was associated with increasing systemic levels of IL-17A or Th17-like cells^{32,52,53},
309 and its inhibition has been proposed as a potential treatment for this disease⁵⁴. TNF is a
310 stereotypical pro-inflammatory cytokine implicated in a plethora of physiological and
311 pathological processes⁵⁵. This cytokine is positively correlated with SARS-CoV-2 viral load³²
312 and the severity of COVID-19 disease⁵³. Moreover, an inverse relationship exists between TNF
313 levels and total T-cell counts in COVID-19 patients⁵⁶. Taken together, these data indicate that
314 SARS-CoV-2 infection not only causes a maternal cytokine response but may also induce fetal
315 inflammation, despite the absence of detectable IgM in the cord blood. Alternatively, the
316 increased concentrations of some cytokines (e.g. IL-8) in the cord blood could be explained by
317 transfer of maternal cytokines through the placental tissues^{57,58}. However, the mechanisms
318 whereby maternal SARS-CoV-2 infection may elicit fetal cytokine responses require further
319 investigation.

320 Importantly, we also report that neonates born to women with SARS-CoV-2 infection
321 had low concentrations of IL-6 in the cord blood. Interleukin-6 is a pleiotropic cytokine, which
322 functions range from hematopoiesis to metabolic regulation of inflammation, autoimmunity, and
323 acute phase response⁵⁹. In viral infections, IL-6 can display pathogenic or protective effects *in*
324 *vivo*⁶⁰, which resembles the functions of this cytokine in pregnancy⁶¹. Consistently, elevated
325 systemic IL-6 levels in patients with SARS-CoV-2 infection are considered to have predictive
326 value for disease severity⁶². In contrast, low levels of this cytokine are associated with good
327 prognosis⁶³. Thus, we suggest that neonates born to asymptomatic pregnant women with SARS-
328 CoV-2 infection display reduced concentrations of IL-6 as a compensatory mechanism to prevent
329 further acute inflammation.

330 A hallmark of SARS-CoV-2 infection is lymphopenia, which is primarily reflected in the
331 T-cell compartment^{53,64-68}, but not consistently observed for B cells⁶⁹. Specifically, patients with
332 symptomatic COVID-19 displayed reduced numbers of CD4⁺ and CD8⁺ T-cell subsets
333 including naïve, central memory, and effector memory cells^{34,66,68,70,71}. Lymphopenia is also
334 correlated with COVID-19 disease severity, as critically ill patients showed the lowest numbers
335 of total lymphocytes, including T-cells, compared to asymptomatic individuals⁷². Yet,
336 asymptomatic or mildly ill pregnant women seem to have slightly reduced lymphocyte numbers
337 when compared to healthy controls⁷³. Indeed, a recent single-center study showed that 80% of
338 pregnant women with mild or asymptomatic SARS-CoV-2 infection displayed lymphopenia⁷⁴.
339 Consistently, we found that pregnant women with SARS-CoV-2 infection had reduced T-cell
340 numbers compared to healthy controls, which included specific subsets such as CD4⁺ T_{CM}, Th1-
341 like, CD8⁺ T_{EM}, and Tc17-like cells. Both Th1 and Tc17 cells participate in orchestrating pro-
342 inflammatory responses in health and disease^{75,76}. During pregnancy, these T-cell subsets are
343 implicated in the establishment and maintenance of maternal-fetal tolerance⁷⁷⁻⁷⁹, which play a
344 central role in pregnancy success⁸⁰⁻⁹⁰. Hence, these results indicate that SARS-CoV-2 infection
345 alters specific pro-inflammatory T-cell subsets in the maternal circulation, which may
346 compromise the mechanisms of maternal-fetal tolerance.

347 Concurrent with the cellular immune changes occurring in the periphery of pregnant
348 women with SARS-CoV-2 infection, maternal T-cell responses in the chorioamniotic
349 membranes were also altered, as revealed by our scRNAseq data. Maternal T cells reside at the
350 maternal-fetal interface and their abundance changes as gestation progresses^{79,91}. This T-cell
351 compartment comprises multiple subsets, including effector/activated T cells, regulatory T cells,
352 and exhausted T cells^{78,92,93}. In addition, these adaptive immune cells can participate in the

353 processes of labor by releasing inflammatory mediators such as TNF, IL-1 β , and MMP-9⁹⁴. The
354 importance of T cells in the process of labor is underscored by observations showing that their
355 single-cell signatures can be detected in the maternal circulation, providing a non-invasive
356 approach to monitor pregnancy and its complications^{39,95}. Consistent with these findings, herein
357 we demonstrated that the single-cell signature of maternal T cells in the chorioamniotic
358 membranes from SARS-CoV-2-infected pregnant women resembled that of peripheral T cells
359 from non-pregnant infected patients (obtained from a previously reported dataset⁴⁰). These
360 results suggest that both systemic and local T-cell responses are altered by SARS-CoV-2; yet,
361 pregnancy also promotes stereotypical cellular responses. Interestingly, maternal T cells from the
362 chorioamniotic membranes displayed enrichment of gene ontology terms related to
363 mitochondrial gene expression and translation, a process that has been implicated in T-cell
364 functions including cytokine production⁹⁶. Therefore, SARS-CoV-2 may enhance maternal T-
365 cell function at the maternal-fetal interface.

366 In the current study, SARS-CoV-2 infection also had effects on maternal macrophages in
367 the chorioamniotic membranes. The processes and pathways enriched in these tissue-resident
368 innate immune cells included response to virus, NOD-like receptor signaling pathway, and
369 cytokine-cytokine receptor interaction, highlighting the role of macrophages in the host response
370 against SARS-CoV-2 infection⁹⁷⁻⁹⁹. Other processes enriched in maternal macrophages included
371 vasculature development and angiogenesis, supporting a role for these cells in the vascular
372 damage to the placentas of women with COVID-19²⁵. Thus, maternal macrophage responses
373 may act as a double-edged sword in the chorioamniotic membranes of women with SARS-CoV-
374 2 infection by modulating host immune responses while simultaneously contributing to placental
375 vasculopathy.

376 Importantly, we report that SARS-CoV-2 infection during pregnancy was neither
377 associated with alterations in the neonatal T-cell repertoire nor with fetal immune responses in
378 the placenta. These observations are in tandem with the absence of SARS-CoV-2
379 transcripts/proteins in the placenta and chorioamniotic membranes as well as undetectable IgM
380 in the cord blood. Our results are in agreement with numerous reports showing that SARS-CoV-
381 2 is undetected in the placenta^{24,100,101}, amniotic fluid¹⁰²⁻¹⁰⁴, and neonates^{5,24,29,102,103}. Yet, SARS-
382 CoV-2 has been reported in the placentas of severe COVID-19 patients^{15,16,23,27,105}, indicating
383 that this virus can on rare occasions reach and infect this organ. Therefore, the absence of SARS-
384 CoV-2 in the chorioamniotic membranes, placental villi, and basal plate of our mostly
385 asymptomatic study population is in accordance with the known scarcity of placental infection
386 ¹⁰⁶.

387 Traditionally, the placenta is considered a sterile organ^{107,108}. Indeed, recent research has
388 reiterated the sterile womb hypothesis using placentas from women who delivered via cesarean
389 section at term without labor¹⁰⁹⁻¹¹¹ as well as studies in mice^{112,113} and non-human primates¹¹⁴.
390 Here, we evaluated the possibility that maternal SARS-CoV-2 infection compromises the
391 sterility of the placenta by facilitating the invasion of bacteria or the transfer of bacterial DNA
392 from maternal compartments. Consistent with our previous studies¹⁰⁹, the placentas of women
393 who delivered via cesarean section did not consistently harbor a microbiome. Women who
394 delivered vaginally displayed placental bacterial signatures similar to those from the lower
395 genital tract; yet, maternal SARS-CoV-2 infection did not modify such signatures. Hence,
396 SARS-CoV-2 infection does not affect placental sterility in mostly asymptomatic women who
397 delivered a term neonate.

398 In summary, we have shown that SARS-CoV-2 infection during pregnancy primarily
399 induces specific maternal inflammatory responses in the periphery and at the maternal-fetal
400 interface, the latter being governed by T cells and macrophages. Maternal SARS-CoV-2
401 infection was also associated with a cytokine response in the neonatal circulation without
402 compromising the cellular immune repertoire. Moreover, SARS-CoV-2 infection during
403 pregnancy neither altered fetal inflammatory responses in the placenta nor induced elevated
404 levels of IgM in the cord blood. Importantly, SARS-CoV-2 was not detected in the placentas of
405 infected women, nor was the sterility of the placenta compromised by this virus. This study
406 provides insight into the maternal-fetal immune responses triggered by SARS-CoV-2 and further
407 emphasizes the rarity of placental infection.

408 **METHODS**

409 *Human subjects, clinical specimens, and definitions*

410 Human maternal peripheral blood, umbilical cord blood, and placental tissues, including
411 chorioamniotic membrane samples, were obtained at the Perinatology Research Branch, an
412 intramural program of the *Eunice Kennedy Shriver* National Institute of Child Health and Human
413 Development (NICHD), National Institutes of Health, U.S. Department of Health and Human
414 Services, Wayne State University (Detroit, MI, USA), and the Detroit Medical Center (DMC)
415 (Detroit, MI, USA). The collection and use of human materials for research purposes were
416 approved by the Institutional Review Boards of Wayne State University School of Medicine,
417 Detroit Medical Center, and NICHD. All participating women provided written informed
418 consent prior to sample collection. The study groups were divided into pregnant women who had
419 a positive RT-PCR test for SARS-CoV-2 (nasopharyngeal test provided by the Detroit Medical
420 Center) and healthy gestational age-matched controls. The demographic and clinical
421 characteristics of the study groups are shown in Supplementary Table 1. The maternal peripheral
422 blood was collected at admission, prior to the administration of any medication, and the
423 umbilical cord blood and placental tissues were collected immediately after delivery.

424 Gestational age was established based on the last menstrual period and confirmed by
425 ultrasound examination. Labor was defined as the presence of regular uterine contractions with a
426 frequency of ≥ 2 times every 10 minutes and cervical ripening. Term delivery was defined as
427 birth ≥ 37 weeks of gestation. Preeclampsia was defined as new-onset hypertension that
428 developed ≥ 20 weeks of gestation and proteinuria¹¹⁵. Other clinical and demographic
429 characteristics were obtained by review of medical records.

430

431 ***Placental histopathological examination***

432 Placentas were examined histologically by perinatal pathologists according to
433 standardized DMC protocols¹¹⁶. Briefly, three to nine sections of the placenta were examined,
434 and at least one full-thickness section was taken from the center of the placenta; others were
435 taken randomly from the placental disc. Acute and chronic inflammatory lesions of the placenta
436 (maternal inflammatory response and fetal inflammatory response), as well as other placental
437 lesions were diagnosed according to established criteria¹¹⁶⁻¹²⁰, as shown in Supplementary Table
438 1.

439

440 ***Immunoassays***

441 ***Immunoglobulin (Ig) M and G determination in the maternal blood and umbilical cord blood***

442 Maternal peripheral blood and umbilical cord blood was collected into tubes without an
443 anticoagulant, and the tubes were stored at room temperature for 30-60 minutes prior to
444 centrifugation for 10 min at 1,600 x g and 4°C. After centrifugation, the serum was collected and
445 stored at -80°C. The serum concentrations of SARS-CoV-2 IgM and IgG were determined using
446 the human anti-SARS-CoV-2 IgM and human anti-SARS-CoV-2 IgG ELISA kits (LifeSpan
447 BioSciences, Inc., Seattle, WA, USA), according to the manufacturer's instructions. Plates were
448 read using the SpectraMax iD5 (Molecular Devices, San Jose, CA, USA) and analyte
449 concentrations were calculated with the SoftMax Pro 7 (Molecular Devices). The sensitivities of
450 the assays were 0.469 ng/mL (human anti-SARS-CoV-2 IgM) and 2.344 ng/mL (human anti-
451 SARS-CoV-2 IgG).

452

453 *Determination of cytokine and chemokine concentrations in the maternal blood and umbilical*
454 *cord blood*

455 Maternal peripheral blood and umbilical cord blood was collected into tubes with an
456 anticoagulant (EDTA or citrate), which were centrifuged for 10 min at 1,600 x g and 4°C. Upon
457 centrifugation, the plasma was collected and stored at -80°C prior to cytokine/chemokine
458 determination. The V-PLEX Pro-Inflammatory Panel 1 (human) and Cytokine Panel 1 (human)
459 immunoassays (Meso Scale Discovery, Rockville, MD, USA) were used to measure the
460 concentrations of IFN- γ , IL-1 β , IL-2, IL-4, IL-6, IL-8, IL-10, IL-12p70, IL-13, and TNF (Pro-
461 inflammatory Panel 1) or GM-CSF, IL-1 α , IL-5, IL-7, IL-12/IL-23p40, IL-15, IL-16, IL-17A,
462 TNF- β , and VEGF-A (Cytokine Panel 1) in the maternal and cord blood plasma, according to the
463 manufacturer's instructions. Plates were read using the MESO QuickPlex SQ 120 (Meso Scale
464 Discovery) and analyte concentrations were calculated with the Discovery Workbench 4.0 (Meso
465 Scale Discovery). The sensitivities of the assays were: 0.21-0.62 pg/mL (IFN- γ), 0.01-0.17
466 pg/mL (IL-1 β), 0.01-0.29 pg/mL (IL-2), 0.01-0.03 pg/mL (IL-4), 0.05-0.09 pg/mL (IL-6), 0.03-
467 0.14 pg/mL (IL-8), 0.02-0.08 pg/mL (IL-10), 0.02-0.89 pg/mL (IL-12p70), 0.03-0.73 pg/mL (IL-
468 13), 0.01-0.13 pg/mL (TNF), 0.08-0.19 pg/mL (GM-CSF), 0.05-2.40 pg/mL (IL-1 α), 0.04-0.46
469 pg/mL (IL-5), 0.08-0.17 pg/mL (IL-7), 0.25-0.42 pg/mL (IL-12/IL-23p40), 0.09-0.25 pg/mL (IL-
470 15), 0.88-9.33 pg/mL (IL-16), 0.19-0.55 pg/mL (IL-17A), 0.04-0.17 pg/mL (TNF- β), 0.55-6.06
471 pg/mL (VEGF-A).

472

473 *Immunophenotyping of maternal and cord blood leukocytes*

474 Maternal peripheral blood and umbilical cord blood was collected into tubes containing
475 EDTA. Fifty μ L of whole blood were incubated with fluorochrome-conjugated anti-human

476 mAbs (Supplementary Table 6) for 30 min at 4°C in the dark. After incubation, erythrocytes
477 were lysed using BD FACS lysing solution (BD Biosciences, San Jose, CA, USA). The resulting
478 leukocytes were washed and resuspended in 0.5 mL of FACS staining buffer (BD Biosciences)
479 and acquired using the BD LSRFortessa flow cytometer and FACSDiva 6.0 software. The
480 absolute number of cells was determined using CountBright absolute counting beads (Thermo
481 Fisher Scientific/Molecular Probes, Eugene, OR, USA). The analysis and figures were
482 performed using the FlowJo software version 10 (FlowJo, Ashland, OR, USA).
483 Immunophenotyping included the identification of: general leukocyte populations (neutrophils,
484 monocytes, T cells, B cells, and NK cells), monocyte subsets, neutrophil subsets, T-cell subsets,
485 and B-cell subsets. Specifically, the numbers of effector memory T cells (T_{EM} ;
486 $CD3^+CD4^+/CD8^+CD45RA^-CCR7^-$), naïve T cells (T_N ; $CD3^+CD4^+/CD8^+CD45RA^+CCR7^+$),
487 central memory T cells (T_{CM} ; $CD3^+CD4^+/CD8^+CD45RA^-CCR7^+$), terminally-differentiated
488 effector memory T cells (T_{EMRA} ; $CD3^+CD4^+/CD8^+CD45RA^+CCR7^-$), Th1/Tc1-like T cells
489 ($CD3^+CD4^+/CD8^+CXCR3^+CCR6^+/CCR6^-$), Th2/Tc2-like T cells
490 ($CD3^+CD4^+/CD8^+CXCR3^-CCR6^-$), and Th17/Tc17-like T cells ($CD3^+CD4^+/CD8^+CXCR3^-$
491 $CCR6^+$) in maternal and cord blood are presented in Fig. 3.

492

493 *Reactive oxygen species (ROS) production by neutrophils and monocytes*

494 Fifty μ L of maternal peripheral blood and cord blood were stimulated with 50 μ L of ROS
495 assay mix containing 1:250 of ROS assay stain and ROS assay buffer [both from the ROS assay
496 Kit (eBioscience, San Diego, CA, USA)], and 1 μ L of phorbol myristate acetate (PMA; 3
497 μ g/mL) (Millipore Sigma, Burlington, MA, USA). The unstimulated group received 1:250 ROS
498 assay mix and 1X phosphate buffered saline (PBS) (Thermo Fisher Scientific/Gibco, Grand

499 Island, NY, USA). The cells were incubated at 37°C with 5% CO₂ for 60 min. Following
500 incubation, erythrocytes were lysed using Ammonium-Chloride-Potassium (ACK) lysing buffer
501 (Lonza, Walkersville, MD, USA), and the resulting leukocytes were collected after
502 centrifugation at 300 x g for 5 min. Next, leukocytes were resuspended in 0.5 mL of 1X PBS and
503 acquired using the BD LSRFortessa flow cytometer and FACSDiva 6.0 software to measure
504 ROS production by neutrophils and monocytes. The analysis and figures were performed using
505 the FlowJo software version 10.

506

507 *Single-cell RNA sequencing*

508 *Preparation of single-cell suspensions*

509 Single-cell suspensions were prepared from the basal plate, placental villi, and
510 chorioamniotic membranes, as previously described with modifications³⁹. Digestion of placental
511 tissues was performed using collagenase A (Sigma Aldrich, St. Louis, MO, USA) or the enzyme
512 cocktail from the Umbilical Cord Dissociation Kit (Miltenyi Biotec, San Diego, CA, USA).
513 Next, tissue suspensions were washed with 1X PBS and filtered through a cell strainer (Miltenyi
514 Biotec). Cell pellets were collected after centrifugation at 300 x g for 10 min at 20°C.
515 Erythrocytes were lysed using ACK lysing buffer and the reaction was stopped by washing with
516 0.04% Bovine Serum Albumin (BSA) (Sigma Aldrich) in 1X PBS. Then, the cell pellets were
517 collected after centrifugation at 300 x g for 10 min at 20°C and resuspended in 1X PBS for cell
518 counting using an automatic cell counter (Cellometer Auto 2000; Nexcelom Bioscience,
519 Lawrence, MA). Dead cells were removed from the cell suspensions using the Dead Cell
520 Removal Kit (Miltenyi Biotec) to obtain a final cell viability of ≥80%.

521

522 *Single-cell library preparation using the 10x Genomics platform*

523 Viable cells were used for single-cell RNAseq library preparation following the protocol
524 for the 10x Genomics Chromium Single Cell 3' Gene Expression Version 3 Kit (10x Genomics,
525 Pleasanton, CA, USA). Briefly, cell suspensions were loaded into the Chromium Controller to
526 generate gel beads in emulsion (GEM), each containing a single cell and a single Gel Bead with
527 barcoded oligonucleotides. Reverse transcription of mRNA into complementary (c)DNA was
528 performed using the Veriti 96-well Thermal Cycler (Thermo Fisher Scientific, Wilmington, DE,
529 USA). The resulting cDNA was purified using Dynabeads MyOne SILANE (10x Genomics) and
530 the SPRIselect Reagent (Beckman Coulter, Indianapolis, IN, USA). cDNA amplicons were
531 optimized via enzymatic fragmentation, end-repair, and A-tailing followed by the incorporation
532 of adaptors and sample index by ligation. The sample index PCR product was amplified using
533 the Veriti 96-well Thermal Cycler. The Agilent Bioanalyzer High Sensitivity Chip (Agilent
534 Santa Clara, CA, USA) was used to analyze and quantify the final library construct. The Kapa
535 DNA Quantification Kit for Illumina platforms (Kapa Biosystems, Wilmington, MA, USA) was
536 used to quantify the DNA libraries, following the manufacturer's instructions.

537

538 *Sequencing*

539 10x scRNAseq libraries were sequenced on the Illumina NextSeq 500 in the Genomics
540 Services Center (GSC) of the Center for Molecular Medicine and Genetics (Wayne State
541 University School of Medicine, Detroit, MI, USA). The Illumina 75 Cycle Sequencing Kit
542 (Illumina, San Diego, CA, USA) was used with 58 cycles for R2, 26 for R1, and 8 for I1.

543

544 *Genotyping*

545 DNA was extracted from maternal peripheral blood and umbilical cord blood/tissue using
546 DNeasy Blood and Tissue Kit (Qiagen, Hilden, Germany), following manufacturer’s instructions
547 modified with the addition of 4 μ l RNase A (100 mg/mL) (Qiagen) and incubation in 56°C.
548 Purified DNA samples were quantified using Qubit™ dsDNA HS Assay Kit (Invitrogen,
549 Carlsbad, CA, USA). Two platforms were used for genotyping: i) low-coverage (~0.4X) whole-
550 genome sequencing imputed to 37.5 M variants using the 1000 Genomes database (Gencove,
551 New York, NY, USA); and ii) Infinium Global Diversity Array-8 v1.0 Kit microarrays processed
552 by the Advanced Genomics Core of University of Michigan (Ann Arbor, MI, USA). For the
553 array platform, genotype information was converted to vcf format using “iaap-cli gencall” and
554 “gtc_to_vcf.py” from Illumina, and imputation to 37.5 M variants using the 1000 Genomes
555 haplotype references was done using the University of Michigan Imputation Server
556 (<https://imputationserver.sph.umich.edu/>). The maternal/fetal relationship of the genotyped
557 samples was ascertained using plink2 KING-robust kinship analysis¹²¹. The vcf files from the
558 two platforms were then merged together and filtered for high quality imputation and coverage
559 for at least ten scRNAseq transcripts using bcftools.

560

561 *scRNAseq data analysis*

562 Sequencing data were processed using Cell Ranger version 4.0.0 from 10x Genomics for
563 de-multiplexing. The fastq files were then aligned using kallisto¹²², and bustools¹²³ summarized
564 the cell/gene transcript counts in a matrix for each sample using the “lamanno” workflow for
565 scRNAseq. Each library was then processed using DIEM¹²⁴ to eliminate debris and empty
566 droplets. In parallel, “cellranger counts” was also used to align the scRNAseq reads using the
567 STAR¹²⁵ aligner to produce the bam files necessary for demultiplexing the individual of origin,

568 based on the genotype information using souporcell¹²⁶ and demuxlet¹²⁷. We removed any
569 droplet/GEM barcode that was assigned to doublet or ambiguous cells in demuxlet or souporcell,
570 and only those cells that could be assigned a pregnancy case and maternal/fetal origin were kept.
571 All count data matrices were then normalized and combined using the “NormalizeData,”
572 “FindVariableFeatures,” and “ScaleData” methods implemented in the Seurat package in R
573 (Seurat version 3.1, R version 4.0.0)^{128,129}. Next, the Seurat “RunPCA” function was applied to
574 obtain the first 100 principal components, and the different libraries were integrated and
575 harmonized using the Harmony package in R version 1.0¹³⁰. The top 30 harmony components
576 were then processed using the Seurat “runUMAP” function to embed and visualize the cells in a
577 two-dimensional map via the Uniform Manifold Approximation and Projection for Dimension
578 Reduction (UMAP) algorithm^{131,132}. To label the cells, the SingleR¹³³ package in R version 1.3.8
579 was used to assign a cell-type identity based on our previously labeled data as reference panel (as
580 performed in³⁹). Cell type abbreviations used are: STB, syncytiotrophoblast; EVT, extravillous
581 trophoblast; CTB, cytotrophoblast; npICTB, non-proliferative interstitial cytotrophoblast; LED,
582 lymphoid endothelial decidual cell; and NK, natural killer cell.

583

584 *Differential gene expression*

585 To identify differentially expressed genes, we created a pseudo-bulk aggregate of all the
586 cells of the same cell-type/location/origin. For each combination, we only used samples with
587 more than 20 cells. The negative binomial model implemented in the DESeq2 R package version
588 1.28.1¹³⁴ was used to calculate the log₂ fold change (FC) between SARS-CoV-2 (+) and healthy
589 pregnant women. The p-values were adjusted using the false discovery rate method (FDR)¹³⁵,
590 and the DEGs were selected based on an adjusted p-value < 0.1. qq-plot was used to assess the

591 distribution of the p-values and to identify which cell types and location combinations have
592 higher enrichment for low p-values. Forest plots were used to visualize the DEGs, with each dot
593 representing the \log_2FC of the SARS-CoV-2 (+) group and the bars representing the 95%
594 confidence interval. The genes with the highest \log_2FC across T-cell, Macrophage-1, and
595 Macrophage-2 cell types were further illustrated using violin plots representing the single-cell
596 gene expression data in \log_{10} [transcripts per million (TPM)].

597

598 *Comparison with previous scRNAseq SARS-CoV-2 studies*

599 Single-cell RNAseq data showing the effects of SARS-CoV-2 on peripheral T cells was
600 obtained from a previous study⁴⁰. The \log_2FC s from this previous study were compared to those
601 obtained here in maternal T cells from the placental villi and basal plate (PVBP) and the
602 chorioamniotic membranes (CAM). The comparison was visualized with scatter plots using the
603 ggplot2 R package version 3.3.2 and Spearman's correlation analysis. Additionally, this
604 previously generated set of SARS-CoV-2-associated genes in T cells was used to repeat the FDR
605 p-value adjustment to reduce the burden of multiple testing in CAM-derived maternal T-cells
606 and provide a longer list of genes. This list of genes was further analyzed with the clusterProfiler
607 in R version 3.16.1 to perform gene set enrichment analysis (GSEA) and over-representation
608 analysis (ORA).

609

610 *Gene ontology and pathway enrichment analysis*

611 The clusterProfiler in R version 3.16.1¹³⁶ was used to perform GSEA and ORA based on
612 the Gene Ontology (GO), Kyoto Encyclopedia of Gene and Genomes (KEGG), and Reactome
613 databases. The ORA determines if biological pathways or processes are enriched in a list of

614 DEGs. GSEA calculates the enrichment score (ES) for each gene set¹³⁷ with respect to the full
615 list of genes ranked by $-\log_{10}(\text{p-value})$. P-values were adjusted for multiple comparisons using
616 the FDR method¹³⁵. The functions “enrichPathway”, “enrichKEGG”, and “gseGO” from
617 “clusterProfiler” were used to perform the ORA and GSEA analyses separately for each list of
618 genes obtained as differentially expressed for each cell type, placental compartment, and
619 maternal/fetal origin. Only results that were significant after correction were reported with $q <$
620 0.05 being considered statistically significant.

621

622 *STRING Analysis*

623 The STRING database (<https://string-db.org>) was utilized to identify and visualize the
624 enrichment of GO terms among all the DEGs, regardless of cell type, compartment, and origin.
625 The STRING database integrates the known and predicted protein-protein associations from
626 many organisms, including both direct (physical) and indirect (functional) interactions¹³⁸. The
627 significant gene ontologies (cellular components) ($q < 0.05$) were selected and highlighted by
628 different colors.

629

630 *Analysis of viral reads in scRNAseq libraries*

631 The R-based computational pipeline Viral-Track was used to study viruses in raw
632 scRNAseq data (github.com/PierreBSC/Viral-Track)⁴¹. A combined index of both the host
633 GRCH37(hg19) and viral reference genomes was constructed in Viral-Track. The viral genomes
634 were downloaded from the Virusite database version 2020.3¹³⁹ that includes all published
635 viruses, viroids, and satellites (NCBI RefSeq). Afterwards, the STAR aligner was used to map
636 reads to the indexed host and viral genome. Viral genomes were filtered based on read-map

637 quality, nucleotide composition, sequence complexity, and genome coverage. Sequence
638 complexity was calculated by computing the average nucleotide frequency and Shannon's
639 entropy. Reads with a sequence entropy above 1.2, genome coverage greater than 5%, and
640 longest contig longer than three times the mean read length are required for a viral segment to be
641 considered present (default thresholds empirically defined by Viral-Track). As no viral reads
642 were detected in our PVBP and CAM libraries, the correct implementation of the Viral-Track
643 pipeline was validated by reanalyzing the data of broncho-alveolar lavage samples of patients
644 with severe and mild SARS-CoV-2⁴¹ and reproducing the detection of SARS-CoV-2 and human
645 metapneumovirus.

646

647 ***Detection of SARS-CoV-2 RNA/proteins in the placenta***

648 *Detection of SARS-CoV-2 RNA in the placenta*

649 Total RNA was isolated from the basal plate, placental villi, and chorioamniotic
650 membranes using QIAshredders and RNeasy Mini Kit (both from Qiagen), according to the
651 manufacturer's instructions. Positive and negative controls were SARS-Related Coronavirus 2
652 (SARS-CoV-2) External Run Control and Negative Control (both from ZeptoMetrix, Buffalo,
653 NY, USA). Following the instructions from the CDC-2019 Novel Coronavirus (2019-nCoV)
654 Real-Time RT-PCR Diagnostic Panel, cDNA was synthesized using TaqPath™ 1-Step RT-
655 qPCR Master Mix, CG (Thermo Fisher Scientific/Applied Biosystems, Frederick, MD, USA)
656 and primers from the 2019-nCoV RUO Kit (Integrated DNA Technologies, Newark, NJ, USA).
657 Reactions were incubated at 25°C for 2 min followed by 50°C for 15 mins. Initial denaturation
658 was set for 2 min at 95°C followed by 45 amplification cycles at 95°C for 3 sec and 55°C for 30
659 sec. A cycle of quantification (C_q value) less than 45 indicates a positive result. Two positive

660 PCR controls were used: 2019-nCoV_N (virus) and Hs_RPP30 (human) (both from Integrated
661 DNA Technologies). Each PCR sample was run in duplicate.

662 RNA extractions were also performed using QIAamp Viral RNA Mini Kit (Qiagen) and
663 results were comparable to those generated using the RNeasy Mini Kit.

664

665 *SARS-CoV-2 Viral Particle Sensitivity Assay*

666 For each experiment (n = 3), ten pieces of freshly collected placental villi from pregnant
667 women were homogenized separately. Nine of the homogenates were spiked with increasing
668 numbers of viral particles [SARS-Related Coronavirus 2 (SARS-CoV-2) External Run Control]
669 (0 to 5,000 particles/homogenate). SARS-Related Coronavirus 2 (SARS-CoV-2) Negative
670 Control was added to the last homogenate prior to mechanical digestion. Total RNA was isolated
671 using the RNeasy Mini Kit, according to manufacturer's instructions. cDNA synthesis and PCR
672 was performed as described above.

673

674 *Detection of SARS-CoV-2 proteins in the placenta*

675 Five- μ m-thick tissue sections of formalin-fixed, paraffin-embedded placental villi (PV),
676 basal plate (BP), and the chorioamniotic membranes (CAM) were cut, mounted on SuperFrost™
677 Plus microscope slides (Erie Scientific LLC, Portsmouth, NH, USA), and subjected to
678 immunohistochemistry using SARS-CoV/SARS-CoV-2 (COVID-19) spike antibody [1A9]
679 (GeneTex, Irvine, CA, USA) and SARS-CoV-2 (COVID-19) nucleocapsid antibody (GeneTex).
680 To serve as a positive control, tissues from pregnant women were spiked with SARS-CoV-2
681 (Isolate: USA/WA1/2020) (ZeptoMetrix) Culture Fluid (heat inactivated). Spiked tissues were
682 subjected to immunohistochemistry using SARS-CoV/SARS-CoV-2 (COVID-19) spike

683 antibody [1A9] and SARS-CoV-2 (COVID-19) nucleocapsid antibody. Staining was performed
684 using the Leica Bond-Max automatic staining system (Leica Microsystems, Wetzlar, Germany)
685 with the Bond Polymer Refine Detection Kit (Leica Microsystems). The mouse isotype (Agilent)
686 and rabbit isotype (Agilent) were used as negative controls. Tissue slides were then scanned
687 using the Vectra Polaris Multispectral Imaging System (Akoya Biosciences, Marlborough, MA,
688 USA) and images were analyzed using the Phenochart v1.0.8 image software (Akoya
689 Biosciences). Supplementary Table 4 summarizes the number of slides included in this study.

690

691 *Detection of SARS-CoV-2 viral RNA in formalin-fixed paraffin-embedded (FFPE) placental*
692 *tissues*

693 From each patient [7 SARS-CoV-2 (+) and 3 healthy pregnant women], 6-14 sections of
694 10- μ m-thick FFPE basal plate, placental villi, and the chorioamniotic membranes were used for
695 total RNA isolation using the PureLink™ FFPE Total RNA Isolation Kit (Invitrogen), according
696 to the manufacturer's instructions. Samples of the basal plate, placental villi, and chorioamniotic
697 membranes were spiked with heat inactivated SARS-Related Coronavirus 2 (SARS-CoV-2)
698 Isolate USA-WA 1/2020 as a positive control prior to formalin fixation and paraffin embedding.
699 Total RNA was isolated from spiked tissues as described above. Following the instructions from
700 the CDC-2019 Novel Coronavirus (2019-nCoV) Real-Time RT-PCR Diagnostic Panel, cDNA
701 was synthesized using TaqPath™ 1-Step RT-qPCR Master Mix, CG and primers from the 2019-
702 nCoV RUO Kit. Reactions were incubated at 25°C for 2 min followed by 50°C for 15 min.
703 Initial denaturation was set for 2 min at 95°C followed by 45 amplification cycles at 95°C for 3
704 sec and 55°C for 30 sec. A cycle of quantification (C_q value) less than 45 indicates a positive

705 result. Two positive PCR controls were used: 2019-nCoV_N (virus) and Hs_RPP30 (human).
706 Each PCR sample was run in duplicate.

707

708 ***Molecular microbiology***

709 *Sample collection*

710 Swabs (FLOQSwabs; COPAN, Murrieta, CA, USA) for molecular microbiology were
711 collected from the chorioamniotic membranes, the amnion-chorion interface of the placental
712 disc, and the placental villous tree. These swabs were stored at -80°C until DNA extractions
713 were performed.

714

715 *DNA extraction*

716 All DNA extractions were completed within a biological safety cabinet using a DNeasy
717 Powerlyzer Powersoil Kit (Qiagen, Germantown, MD, USA), with minor modifications to the
718 manufacturer's instructions as previously described^{112,114}. Personnel wore sterile surgical masks,
719 gowns, and gloves during the procedure. Briefly, following UV treatment, 400 µL of Powerbead
720 solution, 200 µL of phenol:chloroform:isoamyl alcohol (pH 7-8), and 60 µL of pre-heated
721 solution C1 were added to the bead tubes. The swab samples were added to the tubes, incubated
722 for 10 minutes, and then mechanically lysed for two rounds of 30 sec each using a bead beater.
723 Following a 1 min centrifugation and transferring of the supernatant to new tubes, 100 µL of
724 PureLink™ RNase A (20 mg/mL) (Invitrogen), 100 µL of solution C2, and 100 µL of solution
725 C3 were added. The tubes were incubated at 4°C for 5 min and centrifuged for 1 min. After
726 transferring the lysates to new tubes, 650 µL of solution C4 and 650 µL of 100% ethanol were
727 added. Next, 635 µL of the lysate were loaded onto the filter columns and centrifuged for 1 min,

728 discarding the flowthrough. This wash step was repeated three times to ensure all the lysates
729 passed through the columns. Following the washes, 500 μ L of solution C5 were added to the
730 filter columns. After a 1 min centrifugation, the flowthrough was discarded and the tubes were
731 centrifuged again for 2 min to dry the spin columns. The spin columns themselves were
732 transferred to a clean 2.0 mL collection tube, and 60 μ L of pre-heated solution C6 was added
733 directly to the center of the spin columns. After a 5 min incubation at room temperature, the
734 DNA was eluted via a 1 min centrifugation. Purified DNA was then transferred to clean 2.0 mL
735 collection tubes and immediately stored at -20°C. Twelve extractions of sterile FLOQSwabs
736 were included as technical controls for potential background DNA contamination.

737

738 *16s rRNA gene quantitative real-time PCR*

739 Total bacterial DNA abundance within samples was measured via amplification of the V1
740 - V2 region of the 16S rRNA gene according to the protocol of Dickson et al.¹⁴⁰ with minor
741 modifications, as previously described^{112,114}. These modifications included the use of a
742 degenerative forward primer (27f-CM: 5'-AGA GTT TGA TCM TGG CTC AG-3') and a
743 degenerate probe containing locked nucleic acids (+) (BSR65/17: 5'-56FAM-TAA +YA+C ATG
744 +CA+A GT+C GA-BHQ1-3'). Each 20 μ L reaction contained 0.6 μ M of 27f-CM primer, 0.6
745 μ M of 357R primer (5'-CTG CTG CCT YCC GTA G-3'), 0.25 μ M of BSR65/17 probe, 10.0 μ L
746 of 2X TaqMan Environmental Master Mix 2.0 (Invitrogen), and 3.0 μ L of either purified DNA
747 or nuclease-free water. The total bacterial DNA qPCR was performed using the following
748 conditions: 95°C for 10 min, followed by 40 cycles of 94°C for 30 sec, 50°C for 30 sec, and
749 72°C for 30 sec. Duplicate reactions were run for all samples.

750 Raw amplification data were normalized to the ROX passive reference dye and analyzed
751 using the 7500 Software version 2.3 (Applied Biosystems, Foster City, CA, USA) with
752 automatic threshold and baseline settings. Cycle of quantification (Cq) values were calculated for
753 samples based on the mean number of cycles required for normalized fluorescence to
754 exponentially increase.

755

756 *16S rRNA gene sequencing and processing*

757 Amplification and sequencing of the V4 region of the 16S rRNA gene was performed
758 using the dual indexing sequencing strategy developed by Kozich et al.¹⁴¹. The forward primer
759 was 515F: 5'-GTGCCAGCMGCCGCGGTAA-3' and the reverse primer was 806R: 5'-
760 GGACTACHVGGGTWTCTAAT-3'. Each PCR reaction contained 0.75 nM of each primer, 3.0
761 µL template DNA, 10.0 µL of 2X TaqMan Environmental Master Mix 2.0, and DNase-free water
762 to produce a final volume of 20 µL. Reactions were performed using the following conditions:
763 95°C for 10 min, followed by 40 cycles of 95°C for 20 sec, 55°C for 15 sec, and 72°C for 5 min,
764 with an additional elongation at 72°C for 10 min. All PCR reactions were run in duplicate and
765 products from duplicate reactions were pooled prior to purification and sequencing.

766 16S rRNA gene sequencing libraries were prepared according to Illumina's protocol for
767 Preparing Libraries for Sequencing on the MiSeq (15039740 Rev. D) for 2 nM or 4 nM libraries.
768 Sequencing was conducted using the Illumina MiSeq platform (V2 500 cycles, Illumina MS102-
769 2003), according to the manufacturer's instructions with modifications found in¹⁴¹. All samples
770 were quantified using the Qubit dsDNA HS assay and pooled in equimolar concentration prior to
771 sequencing.

772 16S rRNA gene sequences were clustered into amplicon sequence variants (ASVs)

773 defined by 100% sequence similarity using DADA2 version 1.12¹⁴² in R version 3.6.1¹⁴³
774 according to the online MiSeq protocol (<https://benjjneb.github.io/dada2/tutorial.html>) with
775 minor modifications, as previously described¹¹⁴. These modifications included allowing
776 truncation lengths of 250 and 150 bases, and a maximum number of expected errors of 2 and 7
777 bases, for forward and reverse reads, respectively. To increase power for detecting rare variants,
778 sample inference allowed for pooling of samples. Additionally, samples in the resulting sequence
779 table were pooled prior to removal of chimeric sequences. Sequences were then classified using
780 the silva_nr_v132_train_set database with a minimum bootstrap value of 80%, and sequences
781 that were derived from Archaea, chloroplast, or Eukaryota were removed.

782 The R package decontam version 1.6.0¹⁴⁴ was used to identify ASVs that were potential
783 background DNA contaminants based on their pattern of occurrence in biological versus
784 technical control samples using the “IsNotContaminant” function. An ASV was determined to be
785 a contaminant, and was thus removed from the entire dataset, if it had a P score ≥ 0.4 , had a
786 higher mean relative abundance in technical controls than biological samples, and was present in
787 more than one-third of technical control samples. Although one ASV, which was classified as
788 *Lactobacillus*, met all the criteria for being defined as a contaminant, it was highly abundant in
789 all three positive control vaginal samples and was therefore not removed from the dataset.
790 Ultimately, a total of 148 ASVs were determined to be contaminants and were removed from the
791 dataset prior to analysis. The vast majority of these ASVs were classified as *Staphylococcus*
792 (138/148 ASVs; 93.2%).

793

794 *16S rRNA gene profile statistical analyses*

795 Prior to analyses, the dataset was randomly subsampled to 5,426 sequences per sample.

796 Heatmaps of the 16S rRNA gene profiles of samples, including all prominent ASVs (i.e. those
797 ASVs with an average relative abundance $\geq 2\%$ for any placental site and/or mode of delivery
798 combination) were generated using the open-source software program Morpheus
799 (<https://software.broadinstitute.org/morpheus>). Differences in the structure of 16S rRNA gene
800 profiles of samples were assessed using the Bray-Curtis dissimilarity index. Variation in the 16S
801 rRNA gene profiles of the placental samples from different study groups were visualized through
802 Principal Coordinates Analyses (PCoA) using the R package vegan version 2.5-6¹⁴⁵. Statistical
803 evaluation of 16S rRNA gene profile differences between study groups was completed using
804 permutational multivariate analysis of variance (PERMANOVA)¹⁴⁶ through the “adonis”
805 function in the R package vegan version 2.5-6.

806

807 *Statistical analysis*

808 Statistical analyses were performed using SPSS v19.0 (IBM, Armonk, NY, USA) or the
809 R package (as described above). For human demographic data, the group comparisons were
810 performed using the Fisher’s exact test for proportions and Mann-Whitney U-test for non-
811 normally distributed continuous variables. Immunoglobulin and cytokine/chemokine
812 concentrations were compared using Mann-Whitney U-tests. Principal component analysis
813 (PCA) of cytokines detected in all samples was performed using the R package PCAtools after
814 separately normalizing the data from maternal and cord blood. A two-sample student’s t-test was
815 used to assess whether the first principal component (PC1) values were different between SARS-
816 CoV-2-infected and control groups. For the comparison of flow cytometry data between study
817 groups, Mann-Whitney U-tests were also performed. $P < 0.05$ was considered statistically
818 significant. For heatmap representation of immunophenotyping results, flow cytometry data were
819 transformed into Z-scores by subtracting the mean and dividing by the standard deviation, which

820 were both calculated from the control group. The Z-scores were visualized as a heat map and
821 compared between SARS-CoV-2 (+) and control groups using two-sample t-tests. P-values were
822 adjusted for multiple comparisons using the false discovery rate method to obtain q-values. A q-
823 value < 0.1 was considered statistically significant. The principal components (PC) of the flow
824 cytometry data were also determined, and PC1, PC2, and PC3 were plotted on a 3D scatter plot.
825 Single-cell RNAseq and MiSeq data analyses were performed as described in their respective
826 sections.

827

828 **DATA AVAILABILITY**

829 The majority of the data generated in this study are included in the manuscript or in the
830 Supplementary Materials.

831 The genotyping and single-cell RNAseq data reported in this study have been submitted
832 to the NIH dbGAP repository (accession number phs001886.v3.p1). All software and R
833 packages used herein are detailed in the Materials and Methods. Scripts detailing the single-cell
834 analyses are also available at <https://github.com/piquelab/covid19placenta>.

835 The raw MiSeq data reported in this study have been deposited in the NCBI Sequence
836 Read Archive (Bioproject ID: PRJNA701628).

837 **REFERENCES**

- 838 1 CDC. *Data on COVID-19 during Pregnancy*, <[https://www.cdc.gov/coronavirus/2019-](https://www.cdc.gov/coronavirus/2019-ncov/cases-updates/special-populations/pregnancy-data-on-covid-19.html)
839 [ncov/cases-updates/special-populations/pregnancy-data-on-covid-19.html](https://www.cdc.gov/coronavirus/2019-ncov/cases-updates/special-populations/pregnancy-data-on-covid-19.html)> (2021).
- 840 2 Panagiotakopoulos, L. *et al.* SARS-CoV-2 Infection Among Hospitalized Pregnant
841 Women: Reasons for Admission and Pregnancy Characteristics - Eight U.S. Health Care
842 Centers, March 1-May 30, 2020. *MMWR Morb Mortal Wkly Rep* **69**, 1355-1359,
843 doi:10.15585/mmwr.mm6938e2 (2020).
- 844 3 Lokken, E. M. *et al.* Clinical characteristics of 46 pregnant women with a severe acute
845 respiratory syndrome coronavirus 2 infection in Washington State. *Am J Obstet Gynecol*
846 **223**, 911.e911-911.e914, doi:10.1016/j.ajog.2020.05.031 (2020).
- 847 4 Sutton, D., Fuchs, K., D'Alton, M. & Goffman, D. Universal Screening for SARS-CoV-2
848 in Women Admitted for Delivery. *N Engl J Med*, doi:10.1056/NEJMc2009316 (2020).
- 849 5 Chen, L. *et al.* Clinical Characteristics of Pregnant Women with Covid-19 in Wuhan,
850 China. *N Engl J Med*, doi:10.1056/NEJMc2009226 (2020).
- 851 6 Ellington, S. *et al.* Characteristics of Women of Reproductive Age with Laboratory-
852 Confirmed SARS-CoV-2 Infection by Pregnancy Status - United States, January 22-June
853 7, 2020. *MMWR Morb Mortal Wkly Rep* **69**, 769-775, doi:10.15585/mmwr.mm6925a1
854 (2020).
- 855 7 Pierce-Williams, R. A. M. *et al.* Clinical course of severe and critical coronavirus disease
856 2019 in hospitalized pregnancies: a United States cohort study. *Am J Obstet Gynecol*
857 *MF* **2**, 100134, doi:10.1016/j.ajogmf.2020.100134 (2020).
- 858 8 Woodworth, K. R. *et al.* Birth and Infant Outcomes Following Laboratory-Confirmed
859 SARS-CoV-2 Infection in Pregnancy - SET-NET, 16 Jurisdictions, March 29-October

860 14, 2020. *MMWR Morb Mortal Wkly Rep* **69**, 1635-1640,
861 doi:10.15585/mmwr.mm6944e2 (2020).

862 9 Zambrano, L. D. *et al.* Update: Characteristics of Symptomatic Women of Reproductive
863 Age with Laboratory-Confirmed SARS-CoV-2 Infection by Pregnancy Status - United
864 States, January 22-October 3, 2020. *MMWR Morb Mortal Wkly Rep* **69**, 1641-1647,
865 doi:10.15585/mmwr.mm6944e3 (2020).

866 10 CDC. *Investigating the Impact of COVID-19 during Pregnancy*,
867 <[https://www.cdc.gov/coronavirus/2019-ncov/cases-updates/special-](https://www.cdc.gov/coronavirus/2019-ncov/cases-updates/special-populations/pregnancy-data-on-covid-19/what-cdc-is-doing.html)
868 [populations/pregnancy-data-on-covid-19/what-cdc-is-doing.html](https://www.cdc.gov/coronavirus/2019-ncov/cases-updates/special-populations/pregnancy-data-on-covid-19/what-cdc-is-doing.html)> (2021).

869 11 Lokken, E. M. *et al.* Disease Severity, Pregnancy Outcomes and Maternal Deaths among
870 Pregnant Patients with SARS-CoV-2 Infection in Washington State. *Am J Obstet*
871 *Gynecol*, doi:10.1016/j.ajog.2020.12.1221 (2021).

872 12 Lokken, E. M. *et al.* Higher SARS-CoV-2 Infection Rate in Pregnant Patients. *Am J*
873 *Obstet Gynecol*, doi:10.1016/j.ajog.2021.02.011 (2021).

874 13 Raschetti, R. *et al.* Synthesis and systematic review of reported neonatal SARS-CoV-2
875 infections. *Nat Commun* **11**, 5164, doi:10.1038/s41467-020-18982-9 (2020).

876 14 World Health, O. Definition and categorization of the timing of mother-to-child
877 transmission of SARS-CoV-2: scientific brief, 8 February 2021. (World Health
878 Organization, Geneva, 2021).

879 15 Vivanti, A. J. *et al.* Transplacental transmission of SARS-CoV-2 infection. *Nat Commun*
880 **11**, 3572, doi:10.1038/s41467-020-17436-6 (2020).

881 16 Fenizia, C. *et al.* Analysis of SARS-CoV-2 vertical transmission during pregnancy. *Nat*
882 *Commun* **11**, 5128, doi:10.1038/s41467-020-18933-4 (2020).

- 883 17 Schwartz, D. A. & Dhaliwal, A. Infections in pregnancy with COVID-19 and other
884 respiratory RNA virus diseases are rarely, if ever, transmitted to the fetus: Experiences
885 with coronaviruses, HPIV, HMPV RSV, and influenza. *Arch Pathol Lab Med*,
886 doi:10.5858/arpa.2020-0211-SA (2020).
- 887 18 Simmons, G., Zmora, P., Gierer, S., Heurich, A. & Pöhlmann, S. Proteolytic activation of
888 the SARS-coronavirus spike protein: cutting enzymes at the cutting edge of antiviral
889 research. *Antiviral Res* **100**, 605-614, doi:10.1016/j.antiviral.2013.09.028 (2013).
- 890 19 Phillips, J. M., Gallagher, T. & Weiss, S. R. Neurovirulent Murine Coronavirus JHM.SD
891 Uses Cellular Zinc Metalloproteases for Virus Entry and Cell-Cell Fusion. *J Virol* **91**,
892 doi:10.1128/jvi.01564-16 (2017).
- 893 20 Shang, J. *et al.* Structural basis of receptor recognition by SARS-CoV-2. *Nature*,
894 doi:10.1038/s41586-020-2179-y (2020).
- 895 21 Hoffmann, M. *et al.* SARS-CoV-2 Cell Entry Depends on ACE2 and TMPRSS2 and Is
896 Blocked by a Clinically Proven Protease Inhibitor. *Cell* **181**, 271-280 e278,
897 doi:10.1016/j.cell.2020.02.052 (2020).
- 898 22 Pique-Regi, R. *et al.* Does the human placenta express the canonical cell entry mediators
899 for SARS-CoV-2? *Elife* **9**, doi:10.7554/eLife.58716 (2020).
- 900 23 Hecht, J. L. *et al.* SARS-CoV-2 can infect the placenta and is not associated with specific
901 placental histopathology: a series of 19 placentas from COVID-19-positive mothers. *Mod*
902 *Pathol* **33**, 2092-2103, doi:10.1038/s41379-020-0639-4 (2020).
- 903 24 Edlow, A. G. *et al.* Assessment of Maternal and Neonatal SARS-CoV-2 Viral Load,
904 Transplacental Antibody Transfer, and Placental Pathology in Pregnancies During the

905 COVID-19 Pandemic. *JAMA Netw Open* **3**, e2030455,
906 doi:10.1001/jamanetworkopen.2020.30455 (2020).

907 25 Sharps, M. C. *et al.* A structured review of placental morphology and histopathological
908 lesions associated with SARS-CoV-2 infection. *Placenta* **101**, 13-29,
909 doi:10.1016/j.placenta.2020.08.018 (2020).

910 26 Patanè, L. *et al.* Vertical transmission of coronavirus disease 2019: severe acute
911 respiratory syndrome coronavirus 2 RNA on the fetal side of the placenta in pregnancies
912 with coronavirus disease 2019-positive mothers and neonates at birth. *Am J Obstet*
913 *Gynecol MFM* **2**, 100145, doi:10.1016/j.ajogmf.2020.100145 (2020).

914 27 Hosier, H. *et al.* SARS-CoV-2 infection of the placenta. *J Clin Invest* **130**, 4947-4953,
915 doi:10.1172/jci139569 (2020).

916 28 Algarroba, G. N. *et al.* Visualization of severe acute respiratory syndrome coronavirus 2
917 invading the human placenta using electron microscopy. *Am J Obstet Gynecol* **223**, 275-
918 278, doi:10.1016/j.ajog.2020.05.023 (2020).

919 29 Flannery, D. D. *et al.* Assessment of Maternal and Neonatal Cord Blood SARS-CoV-2
920 Antibodies and Placental Transfer Ratios. *JAMA Pediatr*,
921 doi:10.1001/jamapediatrics.2021.0038 (2021).

922 30 Dong, L. *et al.* Possible Vertical Transmission of SARS-CoV-2 From an Infected Mother
923 to Her Newborn. *JAMA*, doi:10.1001/jama.2020.4621 (2020).

924 31 Tay, M. Z., Poh, C. M., Renia, L., MacAry, P. A. & Ng, L. F. P. The trinity of COVID-
925 19: immunity, inflammation and intervention. *Nat Rev Immunol* **20**, 363-374,
926 doi:10.1038/s41577-020-0311-8 (2020).

927 32 Lucas, C. *et al.* Longitudinal analyses reveal immunological misfiring in severe COVID-
928 19. *Nature* **584**, 463-469, doi:10.1038/s41586-020-2588-y (2020).

929 33 Song, J. W. *et al.* Immunological and inflammatory profiles in mild and severe cases of
930 COVID-19. *Nat Commun* **11**, 3410, doi:10.1038/s41467-020-17240-2 (2020).

931 34 Bernardes, J. P. *et al.* Longitudinal Multi-omics Analyses Identify Responses of
932 Megakaryocytes, Erythroid Cells, and Plasmablasts as Hallmarks of Severe COVID-19.
933 *Immunity* **53**, 1296-1314 e1299, doi:10.1016/j.immuni.2020.11.017 (2020).

934 35 Schulte-Schrepping, J. *et al.* Severe COVID-19 Is Marked by a Dysregulated Myeloid
935 Cell Compartment. *Cell* **182**, 1419-1440 e1423, doi:10.1016/j.cell.2020.08.001 (2020).

936 36 Hadjadj, J. *et al.* Impaired type I interferon activity and inflammatory responses in severe
937 COVID-19 patients. *Science* **369**, 718-724, doi:10.1126/science.abc6027 (2020).

938 37 Burton, G. J. & Jauniaux, E. What is the placenta? *Am J Obstet Gynecol* **213**, S6 e1, S6-
939 8, doi:10.1016/j.ajog.2015.07.050 (2015).

940 38 Maltepe, E. & Fisher, S. J. Placenta: the forgotten organ. *Annu Rev Cell Dev Biol* **31**,
941 523-552, doi:10.1146/annurev-cellbio-100814-125620 (2015).

942 39 Pique-Regi, R. *et al.* Single cell transcriptional signatures of the human placenta in term
943 and preterm parturition. *Elife* **8**, doi:10.7554/eLife.52004 (2019).

944 40 Meckiff, B. J. *et al.* Imbalance of Regulatory and Cytotoxic SARS-CoV-2-Reactive
945 CD4(+) T Cells in COVID-19. *Cell* **183**, 1340-1353 e1316,
946 doi:10.1016/j.cell.2020.10.001 (2020).

947 41 Bost, P. *et al.* Host-Viral Infection Maps Reveal Signatures of Severe COVID-19
948 Patients. *Cell* **181**, 1475-1488 e1412, doi:10.1016/j.cell.2020.05.006 (2020).

949 42 Egerup, P. *et al.* Severe Acute Respiratory Syndrome Coronavirus 2 (SARS-CoV-2)
950 Antibodies at Delivery in Women, Partners, and Newborns. *Obstet Gynecol* **137**, 49-55,
951 doi:10.1097/AOG.0000000000004199 (2021).

952 43 Crovetto, F. *et al.* Impact of SARS-CoV-2 Infection on Pregnancy Outcomes: A
953 Population-Based Study. *Clin Infect Dis*, doi:10.1093/cid/ciab104 (2021).

954 44 Simister, N. E., Story, C. M., Chen, H. L. & Hunt, J. S. An IgG-transporting Fc receptor
955 expressed in the syncytiotrophoblast of human placenta. *Eur J Immunol* **26**, 1527-1531,
956 doi:10.1002/eji.1830260718 (1996).

957 45 Leach, J. L. *et al.* Isolation from human placenta of the IgG transporter, FcRn, and
958 localization to the syncytiotrophoblast: implications for maternal-fetal antibody transport.
959 *J Immunol* **157**, 3317-3322 (1996).

960 46 Atyeo, C. *et al.* Compromised SARS-CoV-2-specific placental antibody transfer. *Cell*
961 **184**, 628-642 e610, doi:10.1016/j.cell.2020.12.027 (2021).

962 47 Haider, S. A. Serum IgM in diagnosis of infection in the newborn. *Arch Dis Child* **47**,
963 382-393, doi:10.1136/adc.47.253.382 (1972).

964 48 Guerina, N. G. *et al.* Neonatal serologic screening and early treatment for congenital
965 *Toxoplasma gondii* infection. The New England Regional *Toxoplasma* Working Group.
966 *N Engl J Med* **330**, 1858-1863, doi:10.1056/NEJM199406303302604 (1994).

967 49 Long, Q. X. *et al.* Clinical and immunological assessment of asymptomatic SARS-CoV-2
968 infections. *Nat Med* **26**, 1200-1204, doi:10.1038/s41591-020-0965-6 (2020).

969 50 Miossec, P., Korn, T. & Kuchroo, V. K. Interleukin-17 and type 17 helper T cells. *N Engl*
970 *J Med* **361**, 888-898, doi:10.1056/NEJMra0707449 (2009).

971 51 Liu, Y. *et al.* 2019-novel coronavirus (2019-nCoV) infections trigger an exaggerated
972 cytokine response aggravating lung injury. *ChinaXiv chinaXiv:202002.00018V1* (2020).

973 52 Xu, Z. *et al.* Pathological findings of COVID-19 associated with acute respiratory
974 distress syndrome. *Lancet Respir Med* **8**, 420-422, doi:10.1016/S2213-2600(20)30076-X
975 (2020).

976 53 Huang, C. *et al.* Clinical features of patients infected with 2019 novel coronavirus in
977 Wuhan, China. *Lancet* **395**, 497-506, doi:10.1016/S0140-6736(20)30183-5 (2020).

978 54 Pacha, O., Sallman, M. A. & Evans, S. E. COVID-19: a case for inhibiting IL-17? *Nat*
979 *Rev Immunol* **20**, 345-346, doi:10.1038/s41577-020-0328-z (2020).

980 55 Aggarwal, B. B. Signalling pathways of the TNF superfamily: a double-edged sword. *Nat*
981 *Rev Immunol* **3**, 745-756, doi:10.1038/nri1184 (2003).

982 56 Diao, B. *et al.* Reduction and Functional Exhaustion of T Cells in Patients With
983 Coronavirus Disease 2019 (COVID-19). *Front Immunol* **11**, 827,
984 doi:10.3389/fimmu.2020.00827 (2020).

985 57 Zaretsky, M. V., Alexander, J. M., Byrd, W. & Bawdon, R. E. Transfer of inflammatory
986 cytokines across the placenta. *Obstet Gynecol* **103**, 546-550,
987 doi:10.1097/01.AOG.0000114980.40445.83 (2004).

988 58 Dahlgren, J., Samuelsson, A. M., Jansson, T. & Holmang, A. Interleukin-6 in the
989 maternal circulation reaches the rat fetus in mid-gestation. *Pediatr Res* **60**, 147-151,
990 doi:10.1203/01.pdr.0000230026.74139.18 (2006).

991 59 Tanaka, T., Narazaki, M. & Kishimoto, T. IL-6 in inflammation, immunity, and disease.
992 *Cold Spring Harb Perspect Biol* **6**, a016295, doi:10.1101/cshperspect.a016295 (2014).

993 60 Gubernatorova, E. O., Gorshkova, E. A., Polinova, A. I. & Drutskaya, M. S. IL-6:
994 Relevance for immunopathology of SARS-CoV-2. *Cytokine Growth Factor Rev* **53**, 13-
995 24, doi:10.1016/j.cytogfr.2020.05.009 (2020).

996 61 Prins, J. R., Gomez-Lopez, N. & Robertson, S. A. Interleukin-6 in pregnancy and
997 gestational disorders. *J Reprod Immunol* **95**, 1-14, doi:10.1016/j.jri.2012.05.004 (2012).

998 62 Liu, T. *et al.* The role of interleukin-6 in monitoring severe case of coronavirus disease
999 2019. *EMBO Mol Med* **12**, e12421, doi:10.15252/emmm.202012421 (2020).

1000 63 Zhang, J. *et al.* Serum interleukin-6 is an indicator for severity in 901 patients with
1001 SARS-CoV-2 infection: a cohort study. *J Transl Med* **18**, 406, doi:10.1186/s12967-020-
1002 02571-x (2020).

1003 64 Tavakolpour, S., Rakhshandehroo, T., Wei, E. X. & Rashidian, M. Lymphopenia during
1004 the COVID-19 infection: What it shows and what can be learned. *Immunol Lett* **225**, 31-
1005 32, doi:10.1016/j.imlet.2020.06.013 (2020).

1006 65 Jiang, M. *et al.* T-Cell Subset Counts in Peripheral Blood Can Be Used as Discriminatory
1007 Biomarkers for Diagnosis and Severity Prediction of Coronavirus Disease 2019. *J Infect*
1008 *Dis* **222**, 198-202, doi:10.1093/infdis/jiaa252 (2020).

1009 66 Schub, D. *et al.* High levels of SARS-CoV-2-specific T cells with restricted functionality
1010 in severe courses of COVID-19. *JCI Insight* **5**, doi:10.1172/jci.insight.142167 (2020).

1011 67 Chen, Z. & John Wherry, E. T cell responses in patients with COVID-19. *Nat Rev*
1012 *Immunol* **20**, 529-536, doi:10.1038/s41577-020-0402-6 (2020).

1013 68 Giamarellos-Bourboulis, E. J. *et al.* Complex Immune Dysregulation in COVID-19
1014 Patients with Severe Respiratory Failure. *Cell Host Microbe* **27**, 992-1000 e1003,
1015 doi:10.1016/j.chom.2020.04.009 (2020).

1016 69 Liu, Z. *et al.* Lymphocyte subset (CD4+, CD8+) counts reflect the severity of infection
1017 and predict the clinical outcomes in patients with COVID-19. *J Infect* **81**, 318-356,
1018 doi:10.1016/j.jinf.2020.03.054 (2020).

1019 70 De Biasi, S. *et al.* Marked T cell activation, senescence, exhaustion and skewing towards
1020 TH17 in patients with COVID-19 pneumonia. *Nat Commun* **11**, 3434,
1021 doi:10.1038/s41467-020-17292-4 (2020).

1022 71 Mathew, D. *et al.* Deep immune profiling of COVID-19 patients reveals distinct
1023 immunotypes with therapeutic implications. *Science* **369**, doi:10.1126/science.abc8511
1024 (2020).

1025 72 Zhang, X. *et al.* Viral and host factors related to the clinical outcome of COVID-19.
1026 *Nature* **583**, 437-440, doi:10.1038/s41586-020-2355-0 (2020).

1027 73 Yang, H. *et al.* Clinical features and outcomes of pregnant women suspected of
1028 coronavirus disease 2019. *J Infect* **81**, e40-e44, doi:10.1016/j.jinf.2020.04.003 (2020).

1029 74 Andrikopoulou, M. *et al.* Symptoms and Critical Illness Among Obstetric Patients With
1030 Coronavirus Disease 2019 (COVID-19) Infection. *Obstet Gynecol* **136**, 291-299,
1031 doi:10.1097/AOG.0000000000003996 (2020).

1032 75 Emmi, L. & Romagnani, S. in *The Autoimmune Diseases (Fourth Edition)* (eds Noel R.
1033 Rose & Ian R. Mackay) 83-101 (Academic Press, 2006).

1034 76 Hamada, H. *et al.* Tc17, a unique subset of CD8 T cells that can protect against lethal
1035 influenza challenge. *J Immunol* **182**, 3469-3481, doi:10.4049/jimmunol.0801814 (2009).

1036 77 Saito, S., Nakashima, A., Shima, T. & Ito, M. Th1/Th2/Th17 and regulatory T-cell
1037 paradigm in pregnancy. *Am J Reprod Immunol* **63**, 601-610, doi:10.1111/j.1600-
1038 0897.2010.00852.x (2010).

- 1039 78 Gomez-Lopez, N. *et al.* Regulatory T Cells Play a Role in a Subset of Idiopathic Preterm
1040 Labor/Birth and Adverse Neonatal Outcomes. *Cell Rep* **32**, 107874,
1041 doi:10.1016/j.celrep.2020.107874 (2020).
- 1042 79 Miller, D., Gershater, M., Slutsky, R., Romero, R. & Gomez-Lopez, N. Maternal and
1043 fetal T cells in term pregnancy and preterm labor. *Cell Mol Immunol* **17**, 693-704,
1044 doi:10.1038/s41423-020-0471-2 (2020).
- 1045 80 Chaouat, G., Voisin, G. A., Escalier, D. & Robert, P. Facilitation reaction (enhancing
1046 antibodies and suppressor cells) and rejection reaction (sensitized cells) from the mother
1047 to the paternal antigens of the conceptus. *Clin Exp Immunol* **35**, 13-24 (1979).
- 1048 81 Aluvihare, V. R., Kallikourdis, M. & Betz, A. G. Regulatory T cells mediate maternal
1049 tolerance to the fetus. *Nat Immunol* **5**, 266-271, doi:10.1038/ni1037 (2004).
- 1050 82 Zenclussen, A. C. *et al.* Abnormal T-cell reactivity against paternal antigens in
1051 spontaneous abortion: adoptive transfer of pregnancy-induced CD4⁺CD25⁺ T regulatory
1052 cells prevents fetal rejection in a murine abortion model. *Am J Pathol* **166**, 811-822,
1053 doi:10.1016/s0002-9440(10)62302-4 (2005).
- 1054 83 Robertson, S. A., Guerin, L. R., Moldenhauer, L. M. & Hayball, J. D. Activating T
1055 regulatory cells for tolerance in early pregnancy - the contribution of seminal fluid. *J*
1056 *Reprod Immunol* **83**, 109-116, doi:10.1016/j.jri.2009.08.003 (2009).
- 1057 84 Kahn, D. A. & Baltimore, D. Pregnancy induces a fetal antigen-specific maternal T
1058 regulatory cell response that contributes to tolerance. *Proc Natl Acad Sci U S A* **107**,
1059 9299-9304, doi:10.1073/pnas.1003909107 (2010).

1060 85 Shima, T. *et al.* Regulatory T cells are necessary for implantation and maintenance of
1061 early pregnancy but not late pregnancy in allogeneic mice. *J Reprod Immunol* **85**, 121-
1062 129, doi:10.1016/j.jri.2010.02.006 (2010).

1063 86 Samstein, R. M., Josefowicz, S. Z., Arvey, A., Treuting, P. M. & Rudensky, A. Y.
1064 Extrathymic generation of regulatory T cells in placental mammals mitigates maternal-
1065 fetal conflict. *Cell* **150**, 29-38, doi:10.1016/j.cell.2012.05.031 (2012).

1066 87 Rowe, J. H., Ertelt, J. M., Xin, L. & Way, S. S. Pregnancy imprints regulatory memory
1067 that sustains anergy to fetal antigen. *Nature* **490**, 102-106, doi:10.1038/nature11462
1068 (2012).

1069 88 Matthiesen, L., Kalkunte, S. & Sharma, S. Multiple pregnancy failures: an
1070 immunological paradigm. *Am J Reprod Immunol* **67**, 334-340, doi:10.1111/j.1600-
1071 0897.2012.01121.x (2012).

1072 89 PrabhuDas, M. *et al.* Immune mechanisms at the maternal-fetal interface: perspectives
1073 and challenges. *Nat Immunol* **16**, 328-334, doi:10.1038/ni.3131 (2015).

1074 90 Bonney, E. A. Alternative theories: Pregnancy and immune tolerance. *J Reprod Immunol*
1075 **123**, 65-71, doi:10.1016/j.jri.2017.09.005 (2017).

1076 91 Gomez-Lopez, N., Guilbert, L. J. & Olson, D. M. Invasion of the leukocytes into the
1077 fetal-maternal interface during pregnancy. *J Leukoc Biol* **88**, 625-633,
1078 doi:10.1189/jlb.1209796 (2010).

1079 92 Arenas-Hernandez, M. *et al.* Effector and Activated T Cells Induce Preterm Labor and
1080 Birth That Is Prevented by Treatment with Progesterone. *J Immunol* **202**, 2585-2608,
1081 doi:10.4049/jimmunol.1801350 (2019).

1082 93 Slutsky, R. *et al.* Exhausted and Senescent T Cells at the Maternal-Fetal Interface in
1083 Preterm and Term Labor. *J Immunol Res* **2019**, 3128010, doi:10.1155/2019/3128010
1084 (2019).

1085 94 Gomez-Lopez, N. *et al.* Evidence for a role for the adaptive immune response in human
1086 term parturition. *Am J Reprod Immunol* **69**, 212-230, doi:10.1111/aji.12074 (2013).

1087 95 Tarca, A. L. *et al.* Targeted expression profiling by RNA-Seq improves detection of
1088 cellular dynamics during pregnancy and identifies a role for T cells in term parturition.
1089 *Sci Rep* **9**, 848, doi:10.1038/s41598-018-36649-w (2019).

1090 96 Almeida, L. *et al.* Ribosome-Targeting Antibiotics Impair T Cell Effector Function and
1091 Ameliorate Autoimmunity by Blocking Mitochondrial Protein Synthesis. *Immunity* **54**,
1092 68-83 e66, doi:10.1016/j.immuni.2020.11.001 (2021).

1093 97 Chua, R. L. *et al.* COVID-19 severity correlates with airway epithelium-immune cell
1094 interactions identified by single-cell analysis. *Nat Biotechnol* **38**, 970-979,
1095 doi:10.1038/s41587-020-0602-4 (2020).

1096 98 Liao, M. *et al.* Single-cell landscape of bronchoalveolar immune cells in patients with
1097 COVID-19. *Nat Med* **26**, 842-844, doi:10.1038/s41591-020-0901-9 (2020).

1098 99 Merad, M. & Martin, J. C. Pathological inflammation in patients with COVID-19: a key
1099 role for monocytes and macrophages. *Nat Rev Immunol* **20**, 355-362,
1100 doi:10.1038/s41577-020-0331-4 (2020).

1101 100 Yu, N. *et al.* Clinical features and obstetric and neonatal outcomes of pregnant patients
1102 with COVID-19 in Wuhan, China: a retrospective, single-centre, descriptive study.
1103 *Lancet Infect Dis* **20**, 559-564, doi:10.1016/S1473-3099(20)30176-6 (2020).

- 1104 101 Levitan, D. *et al.* Histologic and Immunohistochemical Evaluation of 65 Placentas from
1105 Women with Polymerase Chain Reaction-proven Severe Acute Respiratory Syndrome
1106 Coronavirus 2 (SARS-CoV-2) Infection. *Arch Pathol Lab Med*, doi:10.5858/arpa.2020-
1107 0793-SA (2021).
- 1108 102 Chen, H. *et al.* Clinical characteristics and intrauterine vertical transmission potential of
1109 COVID-19 infection in nine pregnant women: a retrospective review of medical records.
1110 *Lancet* **395**, 809-815, doi:10.1016/S0140-6736(20)30360-3 (2020).
- 1111 103 Yan, J. *et al.* Coronavirus disease 2019 in pregnant women: a report based on 116 cases.
1112 *Am J Obstet Gynecol* **223**, 111 e111-111 e114, doi:10.1016/j.ajog.2020.04.014 (2020).
- 1113 104 Yu, N. *et al.* No SARS-CoV-2 detected in amniotic fluid in mid-pregnancy. *Lancet Infect*
1114 *Dis* **20**, 1364, doi:10.1016/S1473-3099(20)30320-0 (2020).
- 1115 105 Cribru, F. M. *et al.* Severe SARS-CoV-2 placenta infection can impact neonatal outcome
1116 in the absence of vertical transmission. *J Clin Invest*, doi:10.1172/JCI145427 (2021).
- 1117 106 Kotlyar, A. M. *et al.* Vertical transmission of coronavirus disease 2019: a systematic
1118 review and meta-analysis. *Am J Obstet Gynecol* **224**, 35-53 e33,
1119 doi:10.1016/j.ajog.2020.07.049 (2021).
- 1120 107 Funkhouser, L. J. & Bordenstein, S. R. Mom knows best: the universality of maternal
1121 microbial transmission. *PLoS Biol* **11**, e1001631, doi:10.1371/journal.pbio.1001631
1122 (2013).
- 1123 108 Perez-Munoz, M. E., Arrieta, M. C., Ramer-Tait, A. E. & Walter, J. A critical assessment
1124 of the "sterile womb" and "in utero colonization" hypotheses: implications for research
1125 on the pioneer infant microbiome. *Microbiome* **5**, 48, doi:10.1186/s40168-017-0268-4
1126 (2017).

1127 109 Theis, K. R. *et al.* Does the human placenta delivered at term have a microbiota? Results
1128 of cultivation, quantitative real-time PCR, 16S rRNA gene sequencing, and
1129 metagenomics. *Am J Obstet Gynecol* **220**, 267 e261-267 e239,
1130 doi:10.1016/j.ajog.2018.10.018 (2019).

1131 110 de Goffau, M. C. *et al.* Human placenta has no microbiome but can contain potential
1132 pathogens. *Nature* **572**, 329-334, doi:10.1038/s41586-019-1451-5 (2019).

1133 111 Sterpu, I. *et al.* No evidence for a placental microbiome in human pregnancies at term.
1134 *Am J Obstet Gynecol*, doi:10.1016/j.ajog.2020.08.103 (2020).

1135 112 Theis, K. R. *et al.* No Consistent Evidence for Microbiota in Murine Placental and Fetal
1136 Tissues. *mSphere* **5**, doi:10.1128/mSphere.00933-19 (2020).

1137 113 Kuperman, A. A. *et al.* Deep microbial analysis of multiple placentas shows no evidence
1138 for a placental microbiome. *BJOG* **127**, 159-169, doi:10.1111/1471-0528.15896 (2020).

1139 114 Theis, K. R., Romero, R., Winters, A. D., Jobe, A. H. & Gomez-Lopez, N. Lack of
1140 Evidence for Microbiota in the Placental and Fetal Tissues of Rhesus Macaques. *mSphere*
1141 **5**, doi:10.1128/mSphere.00210-20 (2020).

1142 115 ACOG. Gestational Hypertension and Preeclampsia: ACOG Practice Bulletin, Number
1143 222. *Obstet Gynecol* **135**, e237-e260, doi:10.1097/AOG.0000000000003891 (2020).

1144 116 Khong, T. Y. *et al.* Sampling and Definitions of Placental Lesions: Amsterdam Placental
1145 Workshop Group Consensus Statement. *Arch Pathol Lab Med* **140**, 698-713,
1146 doi:10.5858/arpa.2015-0225-CC (2016).

1147 117 Kim, C. J. *et al.* Acute chorioamnionitis and funisitis: definition, pathologic features, and
1148 clinical significance. *Am J Obstet Gynecol* **213**, S29-52, doi:10.1016/j.ajog.2015.08.040
1149 (2015).

1150 118 Redline, R. W. Classification of placental lesions. *Am J Obstet Gynecol* **213**, S21-28,
1151 doi:10.1016/j.ajog.2015.05.056 (2015).

1152 119 Kim, C. J., Romero, R., Chaemsaitong, P. & Kim, J. S. Chronic inflammation of the
1153 placenta: definition, classification, pathogenesis, and clinical significance. *Am J Obstet*
1154 *Gynecol* **213**, S53-69, doi:10.1016/j.ajog.2015.08.041 (2015).

1155 120 Romero, R. *et al.* The frequency and type of placental histologic lesions in term
1156 pregnancies with normal outcome. *J Perinat Med* **46**, 613-630, doi:10.1515/jpm-2018-
1157 0055 (2018).

1158 121 Manichaikul, A. *et al.* Robust relationship inference in genome-wide association studies.
1159 *Bioinformatics* **26**, 2867-2873, doi:10.1093/bioinformatics/btq559 (2010).

1160 122 Bray, N. L., Pimentel, H., Melsted, P. & Pachter, L. Near-optimal probabilistic RNA-seq
1161 quantification. *Nat Biotechnol* **34**, 525-527, doi:10.1038/nbt.3519 (2016).

1162 123 Melsted, P. *et al.* Modular and efficient pre-processing of single-cell RNA-seq. *bioRxiv*,
1163 673285, doi:10.1101/673285 (2019).

1164 124 Alvarez, M. *et al.* Enhancing droplet-based single-nucleus RNA-seq resolution using the
1165 semi-supervised machine learning classifier DIEM. *Sci Rep* **10**, 11019,
1166 doi:10.1038/s41598-020-67513-5 (2020).

1167 125 Dobin, A. *et al.* STAR: ultrafast universal RNA-seq aligner. *Bioinformatics* **29**, 15-21,
1168 doi:10.1093/bioinformatics/bts635 (2013).

1169 126 Heaton, H. *et al.* Souporecell: robust clustering of single-cell RNA-seq data by genotype
1170 without reference genotypes. *Nat Methods* **17**, 615-620, doi:10.1038/s41592-020-0820-1
1171 (2020).

1172 127 Kang, H. M. *et al.* Multiplexed droplet single-cell RNA-sequencing using natural genetic
1173 variation. *Nat Biotechnol* **36**, 89-94, doi:10.1038/nbt.4042 (2018).

1174 128 Hafemeister, C. & Satija, R. Normalization and variance stabilization of single-cell RNA-
1175 seq data using regularized negative binomial regression. *Genome Biol* **20**, 296,
1176 doi:10.1186/s13059-019-1874-1 (2019).

1177 129 Stuart, T. *et al.* Comprehensive Integration of Single-Cell Data. *Cell* **177**, 1888-1902
1178 e1821, doi:10.1016/j.cell.2019.05.031 (2019).

1179 130 Korsunsky, I. *et al.* Fast, sensitive and accurate integration of single-cell data with
1180 Harmony. *Nat Methods* **16**, 1289-1296, doi:10.1038/s41592-019-0619-0 (2019).

1181 131 McInnes, L., Healy, J. & Melville, J. UMAP: Uniform Manifold Approximation and
1182 Projection for Dimension Reduction. arXiv:1802.03426 (2018).
1183 <<https://ui.adsabs.harvard.edu/abs/2018arXiv180203426M>>.

1184 132 Becht, E. *et al.* Dimensionality reduction for visualizing single-cell data using UMAP.
1185 *Nat Biotechnol*, doi:10.1038/nbt.4314 (2018).

1186 133 Aran, D. *et al.* Reference-based analysis of lung single-cell sequencing reveals a
1187 transitional profibrotic macrophage. *Nat Immunol* **20**, 163-172, doi:10.1038/s41590-018-
1188 0276-y (2019).

1189 134 Love, M. I., Huber, W. & Anders, S. Moderated estimation of fold change and dispersion
1190 for RNA-seq data with DESeq2. *Genome Biol* **15**, 550, doi:10.1186/s13059-014-0550-8
1191 (2014).

1192 135 Benjamini, Y. & Hochberg, Y. Controlling the false discovery rate: a practical and
1193 powerful approach to multiple testing. *J Roy Statist Soc Ser B* **57**, 289-300 (1995).

1194 136 Yu, G., Wang, L. G., Han, Y. & He, Q. Y. clusterProfiler: an R package for comparing
1195 biological themes among gene clusters. *OMICS* **16**, 284-287, doi:10.1089/omi.2011.0118
1196 (2012).

1197 137 Subramanian, A. *et al.* Gene set enrichment analysis: a knowledge-based approach for
1198 interpreting genome-wide expression profiles. *Proc Natl Acad Sci U S A* **102**, 15545-
1199 15550, doi:10.1073/pnas.0506580102 (2005).

1200 138 Szklarczyk, D. *et al.* The STRING database in 2017: quality-controlled protein-protein
1201 association networks, made broadly accessible. *Nucleic Acids Res* **45**, D362-D368,
1202 doi:10.1093/nar/gkw937 (2017).

1203 139 Stano, M., Beke, G. & Klucar, L. viruSITE-integrated database for viral genomics.
1204 *Database (Oxford)* **2016**, doi:10.1093/database/baw162 (2016).

1205 140 Dickson, R. P. *et al.* Changes in the lung microbiome following lung transplantation
1206 include the emergence of two distinct *Pseudomonas* species with distinct clinical
1207 associations. *PLoS One* **9**, e97214, doi:10.1371/journal.pone.0097214 (2014).

1208 141 Kozich, J. J., Westcott, S. L., Baxter, N. T., Highlander, S. K. & Schloss, P. D.
1209 Development of a dual-index sequencing strategy and curation pipeline for analyzing
1210 amplicon sequence data on the MiSeq Illumina sequencing platform. *Appl Environ*
1211 *Microbiol* **79**, 5112-5120, doi:10.1128/AEM.01043-13 (2013).

1212 142 Callahan, B. J. *et al.* DADA2: High-resolution sample inference from Illumina amplicon
1213 data. *Nat Methods* **13**, 581-583, doi:10.1038/nmeth.3869 (2016).

1214 143 R: A language and environment for statistical computing (R Foundation for Statistical
1215 Computing, Vienna, Austria, 2019).

1216 144 Davis, N. M., Proctor, D. M., Holmes, S. P., Relman, D. A. & Callahan, B. J. Simple
1217 statistical identification and removal of contaminant sequences in marker-gene and
1218 metagenomics data. *Microbiome* **6**, 226, doi:10.1186/s40168-018-0605-2 (2018).
1219 145 vegan: Community ecology package v. 2.5-6 (2019).
1220 146 Anderson, M. J. in *Wiley StatsRef: Statistics Reference Online* 1-15.
1221

1222 **ACKNOWLEDGEMENTS**

1223 We thank the physicians, nurses, and research assistants from the Center for Advanced
1224 Obstetrical Care and Research, Intrapartum Unit, Perinatology Research Branch Clinical
1225 Laboratory, and Perinatology Research Branch Perinatal Translational Science Laboratory for
1226 help with collecting samples. This research was supported, in part, by the Perinatology Research
1227 Branch, Division of Obstetrics and Maternal-Fetal Medicine, Division of Intramural Research,
1228 *Eunice Kennedy Shriver* National Institute of Child Health and Human Development, National
1229 Institutes of Health, U.S. Department of Health and Human Services (NICHD/NIH/DHHS); and,
1230 in part, with Federal funds from NICHD/NIH/DHHS under Contract No.
1231 HHSN275201300006C. This research was also supported by the Wayne State University
1232 Perinatal Initiative in Maternal, Perinatal and Child Health. R.R. has contributed to this work as
1233 part of his official duties as an employee of the United States Federal Government.

1234

1235 **AUTHOR CONTRIBUTIONS**

1236 V.G.-F., performed experiments, analyzed data, and wrote the manuscript. N.G.-L.
1237 conceived, designed, and supervised the study, provided intellectual input, and wrote the
1238 manuscript. R.R. conceived and supervised the study, provided intellectual input, and wrote the
1239 manuscript. R.P.-R., Y.X., and K.T. designed the study, analyzed data, provided intellectual
1240 input, and wrote the manuscript. M.A.-H., D.M., A.P., J.G., M.G., and E.P. performed
1241 experiments or analyzed data, and drafted the manuscript. D.L., D.K., V.F., Y.L., L.T., M.F., and
1242 G.Z. performed experiments or analyzed data. G.B. and A.L.T. analyzed data, provided
1243 intellectual input, and drafted the manuscript. R.P. and C.-D.H., provided human samples used in
1244 the study and intellectual input. All authors revised and provided feedback for the final version
1245 of the manuscript.

1246 **DECLARATION OF INTERESTS**

1247 The authors declare no competing interests.

1248

1249 **MATERIALS AND CORRESPONDENCE**

1250 Correspondence and requests for materials should be addressed to N.G-L.

1251

1252 **FIGURE LEGENDS**

1253 **Figure 1. Serological and cytokine responses in pregnant women with SARS-CoV-2**

1254 **infection and their neonates. (A)** Serum concentrations of IgM and IgG in the maternal
1255 peripheral blood (n = 7 per group) (left panel) and cord blood (n = 4-5 per group) (right panel)
1256 from SARS-CoV-2 (+) or healthy pregnant women. Bar plots represent mean and standard error
1257 of the mean. Differences between two groups were evaluated by Mann-Whitney U tests. **(B)**
1258 Plasma concentrations of IL-6, IL-15, IL-17A, IFN- γ , and TNF in the maternal peripheral blood
1259 (n = 6-7 per group). Blue dots indicate healthy pregnant women, light red dots indicate SARS-
1260 CoV-2 (+) pregnant women, and the dark red dot indicates one patient with severe COVID-19
1261 disease. **(C)** Plasma concentrations of IL-6, IL-15, IL-17A, IFN- γ , and TNF in the cord blood (n
1262 = 5-7 per group). Blue dots indicate healthy pregnant women, light red dots indicate SARS-CoV-
1263 2 (+) pregnant women, and the dark red dot indicates one patient with severe COVID-19 disease.
1264 **(D)** Scatter plot of the first two principal components (PC1 and PC2) from cytokine
1265 concentrations in the maternal plasma. Blue dots indicate healthy pregnant women and red dots
1266 indicate SARS-CoV-2 (+) pregnant women. **(E)** Scatter plot of PC1 and PC2 from cytokine
1267 concentrations in the cord blood plasma. Blue dots indicate healthy pregnant women and red dots
1268 indicate SARS-CoV-2 (+) pregnant women. Bar plots represent mean and standard error of the
1269 mean. Differences in cytokine concentrations between groups were evaluated by Mann-Whitney
1270 U-tests. Differences in PC1 values between SARS-CoV-2 (+) and healthy pregnant women were
1271 assessed using two-sample student's t-tests. P values are considered significant when $p < 0.05$.

1272

1273 **Figure 2. Immunophenotyping of T cells in pregnant women with SARS-CoV-2 infection**

1274 **and their neonates. (A)** Maternal peripheral blood and cord blood were collected for

1275 immunophenotyping by flow cytometry. **(B)** Numbers of T cells in the maternal blood (n = 7-8
1276 per group) and cord blood (n = 6-7 per group) from SARS-CoV-2 (+) or healthy pregnant
1277 women. Bar plots represent mean and standard error of the mean. Differences between groups
1278 were evaluated by Mann-Whitney U-tests. P values < 0.05 were used to denote a significant
1279 result. Blue dots indicate healthy pregnant women, light red dots indicate SARS-CoV-2 (+)
1280 pregnant women, and the dark red dot indicates one patient with severe COVID-19 disease. **(C)**
1281 Heatmap showing abundance (z-scores) for T cell subsets in the maternal blood from SARS-
1282 CoV-2 (+) or healthy pregnant women (n = 7-8 per group). Cell numbers and proportions are
1283 shown. Differences between groups were assessed using two-sample t-tests. P values were
1284 adjusted for multiple comparisons using false discovery rate (FDR) method to obtain q values. *
1285 q < 0.1; ** q < 0.05. Red and green indicate increased and decreased abundance, respectively.
1286 **(D)** Three-dimensional scatter plot showing the distribution of flow cytometry data from the
1287 maternal blood of SARS-CoV-2 (+) (red dots) or healthy pregnant women (blue dots) (n = 7-8
1288 per group) based on principal component (PC)1, PC2, and PC3.

1289

1290 **Figure 3. T cell subsets in pregnant women with SARS-CoV-2 infection and their neonates.**

1291 **(A)** Representative gating strategy used to identify CD4⁺ and CD8⁺ T cells, and their respective
1292 subsets, within the total T cell population (CD45⁺CD3⁺ cells) in the maternal blood and cord
1293 blood. **(B)** Numbers of CD4⁺ T cells, CD4⁺ T_{CM}, CXCR3⁺CCR6⁺ Th1-like cells, and
1294 CXCR3⁺CCR6⁻ Th1-like cells (upper row); and the numbers of CD8⁺ T cells, CD8⁺ T_{CM}, CD8⁺
1295 T_{EM}, and Tc17-like cells (lower row) in the maternal blood from SARS-CoV-2 (+) or healthy
1296 pregnant women (n = 7-8). **(C)** Numbers of CD4⁺ T cells, CD4⁺ T_{CM}, CXCR3⁺CCR6⁺ Th1-like
1297 cells, and CXCR3⁺CCR6⁻ Th1-like cells (upper row); and the numbers of CD8⁺ T cells, CD8⁺

1298 T_{CM}, CD8⁺ T_{EM}, and Tc17-like cells (lower row) in the cord blood from SARS-CoV-2 (+) or
1299 healthy pregnant women (n = 6-7 per group). Bar plots represent mean and standard error of the
1300 mean. Differences between groups were evaluated by Mann-Whitney U-tests, with p < 0.05
1301 being considered significant. Blue dots indicate healthy pregnant women, light red dots indicate
1302 SARS-CoV-2 (+) women, and the dark red dot indicates one patient with severe COVID-19
1303 disease.

1304

1305 **Figure 4. Single-cell RNA sequencing of the placental tissues of women with SARS-CoV-2**
1306 **infection. (A)** Uniform Manifold Approximation Plot (UMAP) showing the combined cell type
1307 classifications from the chorioamniotic membranes (CAM) and placental villi and basal plate
1308 (PVBP) of SARS-CoV-2 (+) or healthy pregnant women (n = 7-8 per group), where each dot
1309 represents a single cell. Abbreviations used are: CTB, cytotrophoblast; EVT, extravillous
1310 trophoblast; LED, lymphoid endothelial decidual cell; npICTB, non-proliferative interstitial
1311 cytotrophoblast; STB, syncytiotrophoblast. **(B)** UMAP showing cell populations separated based
1312 on placental compartment (CAM and PVBP) from SARS-CoV-2 (+) or healthy pregnant women.
1313 **(C)** Bar plot showing the numbers of cells of each type in the CAM and PVBP of SARS-CoV-2
1314 (+) or healthy pregnant women. **(D)** Number of differentially expressed genes (DEG) in each cell
1315 type from the CAM and PVBP with false discovery rate (FDR) adjusted p < 0.1. **(E)** Quantile-
1316 quantile (Q-Q) plot showing differential expression of all tested genes in each cell type of
1317 maternal or fetal origin from the CAM and PVBP samples. Deviation above the 1:1 line (solid
1318 black line) indicates enrichment.

1319

1320 **Figure 5. Single-cell characterization of T cells and macrophages from the chorioamniotic**
1321 **membranes (CAM) and placental villi and basal plate (PVBP).** (A) Scatter plots showing the
1322 effects of SARS-CoV-2 on gene expression [\log_2 Fold Change (FC)] in T cells from the CAM
1323 and PVBP compared to a previously reported dataset⁴⁰. Black dots represent genes with nominal
1324 $p < 0.01$ in this study, which are used to calculate Spearman's correlation. (B) Forest plot
1325 showing differentially expressed genes in T cell, macrophage-2, macrophage-1, monocyte,
1326 lymphoid endothelial decidual cell (LED), cytotrophoblast (CTB), non-proliferative interstitial
1327 cytotrophoblast (npiCTB), and stromal-3 cell populations in the CAM and PVBP of SARS-CoV-
1328 2 (+) or healthy pregnant women ($n = 7-8$ per group). Differentially expressed genes shown are
1329 significant after false discovery rate (FDR) adjustment ($q < 0.1$). (C) Violin plot showing the
1330 distribution of single-cell gene expression levels for the top three upregulated and downregulated
1331 genes in the maternal T cell, macrophage-1, and macrophage-2 populations in the CAM
1332 comparing between SARS-CoV-2 (+) and healthy pregnant women ($n = 7-8$ per group). (D)
1333 Gene ontology (GO) terms enriched in differentially expressed genes in the macrophage-1 and T
1334 cell populations of maternal (M) origin from CAM samples. GO terms with $q < 0.05$ are shown.
1335 (E) Kyoto Encyclopedia of Gene and Genomes (KEGG) pathways enriched for differentially
1336 expressed genes in macrophage-2 of maternal (M) origin from the CAM based on the over-
1337 representation analysis. KEGG pathways with $q < 0.05$ were selected.

1338

1339 **Figure 6. Immunohistological and molecular detection of SARS-CoV-2 proteins/RNA in the**
1340 **placenta of women with SARS-CoV-2 infection.** (A) Schematic representation showing
1341 various sampling locations in the placental villi (PV), basal plate (BP), and chorioamniotic
1342 membranes (CAM) that were tested for SARS-CoV-2 proteins/RNA by immunohistochemistry

1343 and RT-qPCR, respectively. **(B)** Brightfield microscopy images showing positive signal for
1344 SARS-CoV-2 spike (left panel) and nucleocapsid (right panel) proteins in the PV, BP, and CAM
1345 of spike-in positive control. Brown color indicates putative positive staining. **(C)** Brightfield
1346 microscopy images showing putative positive signal for SARS-CoV-2 spike (left panel) and
1347 nucleocapsid (right panel) proteins in the PV, BP, and CAM of a SARS-CoV-2 (+) pregnant
1348 woman. **(D)** Brightfield microscopy images showing negative signal for SARS-CoV-2 spike (left
1349 panel) and nucleocapsid (right panel) proteins in the PV, BP, and CAM of SARS-CoV-2 (+)
1350 pregnant women. **(E)** Brightfield microscopy images showing negative signal for SARS-CoV-2
1351 spike (left panel) and nucleocapsid (right panel) proteins in the PV, BP, and CAM of healthy
1352 pregnant women. **(F)** RT-qPCR results of SARS-CoV-2 viral RNA detection in the PV, BP, and
1353 CAM from formalin-fixed paraffin-embedded tissues from SARS-CoV-2 (+) and healthy
1354 pregnant women. N1 and N2 denote two SARS-CoV-2 nucleocapsid (N) genes, and RP denotes
1355 RNase P gene, which serves as a positive internal PCR control. Spike-in positive controls are
1356 also included. Undetermined quantification cycle (C_q) values are represented below the detection
1357 limit (gray area).

1358

1359 **Figure 7. Bacterial DNA profiles of the placental tissues from pregnant women with SARS-**
1360 **CoV-2 infection. (A)** Schematic representation of sampling locations from the chorioamniotic
1361 membranes (CAM), amnion-chorion interface of the placenta (AC), and within the placental
1362 villous tree (VT) from SARS-CoV-2 (+) women who delivered by cesarean section ($n = 2$) or
1363 vaginally ($n = 5$) and from healthy pregnant women who delivered by cesarean section ($n = 3$) or
1364 vaginally ($n = 5$). **(B)** Quantitative real-time PCR analyses illustrating the bacterial loads (i.e.
1365 16S rDNA abundance) of the CAM, AC, and VT from SARS-CoV-2 (+) or healthy pregnant

1366 women (cesarean section or vaginal delivery). The solid black line denotes the lowest cycle of
1367 quantification (i.e. highest bacterial load) for any blank DNA extraction kit negative control.
1368 Data from three human vaginal swabs are included for perspective. **(C)** Heatmap illustrating the
1369 relative abundances of prominent (>2% average relative abundance) amplicon sequence variants
1370 (ASVs) among the 16S rRNA gene profiles of the CAM, AC, and VT from SARS-CoV-2 (+) or
1371 healthy pregnant women (cesarean section or vaginal delivery). Data from blank DNA extraction
1372 kit negative controls and human vaginal swabs are included for perspective. **(D)** Principal
1373 coordinates analyses (PCoA) illustrating similarity in the 16S rRNA gene profiles of the CAM,
1374 AC, and VT obtained through vaginal delivery from SARS-CoV-2 (+) or healthy pregnant
1375 women.

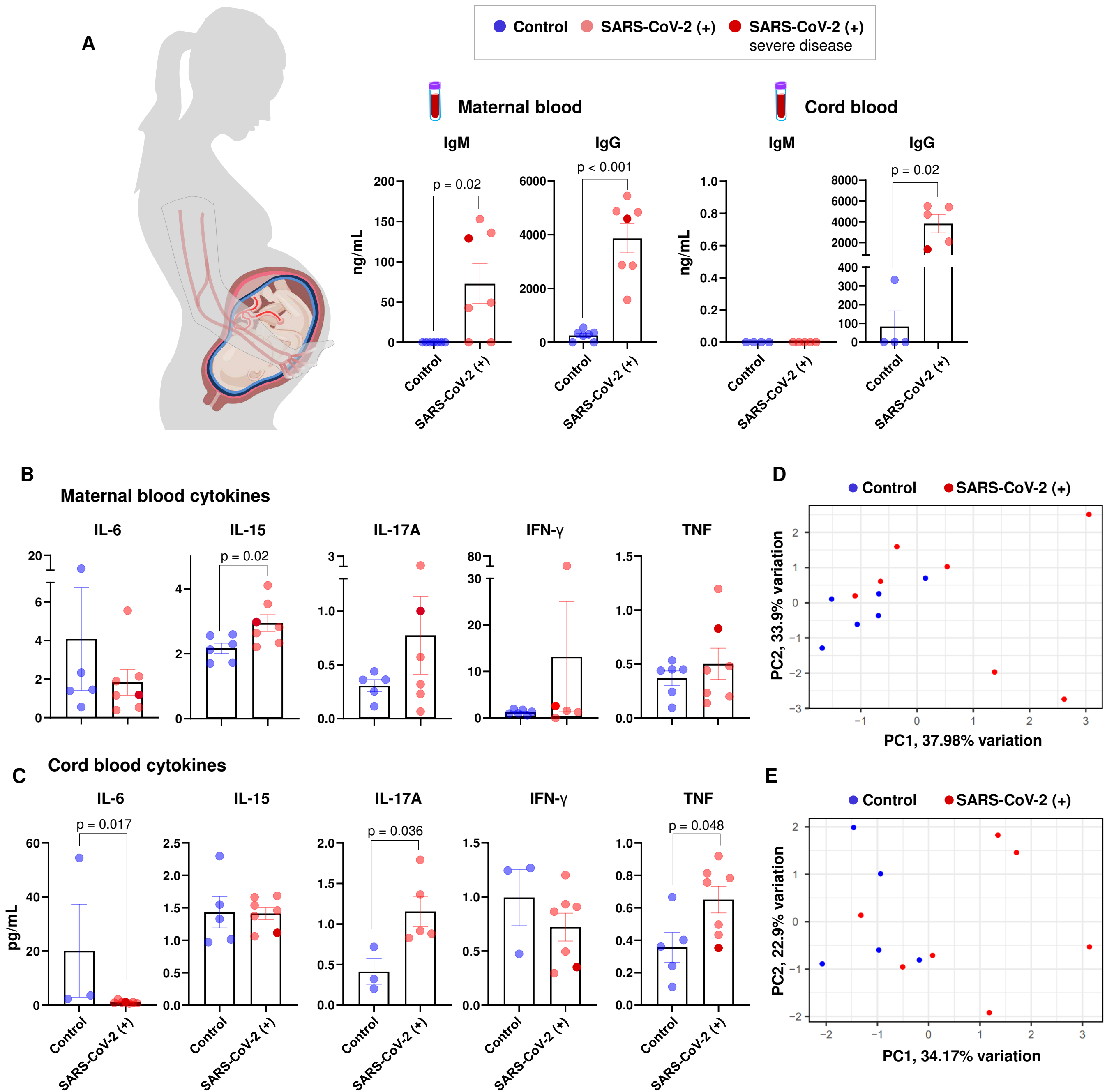


Figure 1. Serological and cytokine responses in pregnant women with SARS-CoV-2 infection and their neonates. (A) Serum concentrations of IgM and IgG in the maternal peripheral blood ($n = 7$ per group) (left panel) and cord blood ($n = 4-5$ per group) (right panel) from SARS-CoV-2 (+) or healthy pregnant women. Bar plots represent mean and standard error of the mean. Differences between two groups were evaluated by Mann-Whitney U tests. **(B)** Plasma concentrations of IL-6, IL-15, IL-17A, IFN- γ , and TNF in the maternal peripheral blood ($n = 6-7$ per group). Blue dots indicate healthy pregnant women, light red dots indicate SARS-CoV-2 (+) pregnant women, and the dark red dot indicates one patient with severe COVID-19 disease. **(C)** Plasma concentrations of IL-6, IL-15, IL-17A, IFN- γ , and TNF in the cord blood ($n = 5-7$ per group). Blue dots indicate healthy pregnant women, light red dots indicate SARS-CoV-2 (+) pregnant women, and the dark red dot indicates one patient with severe COVID-19 disease. **(D)** Scatter plot of the first two principal components (PC1 and PC2) from cytokine concentrations in the maternal plasma. Blue dots indicate healthy pregnant women and red dots indicate SARS-CoV-2 (+) pregnant women. **(E)** Scatter plot of PC1 and PC2 from cytokine concentrations in the cord blood plasma. Blue dots indicate healthy pregnant women and red dots indicate SARS-CoV-2 (+) pregnant women. Bar plots represent mean and standard error of the mean. Differences in cytokine concentrations between groups were evaluated by Mann-Whitney U-tests. Differences in PC1 values between SARS-CoV-2 (+) and healthy pregnant women were assessed using two-sample student's t-tests. P values are considered significant when $p < 0.05$.

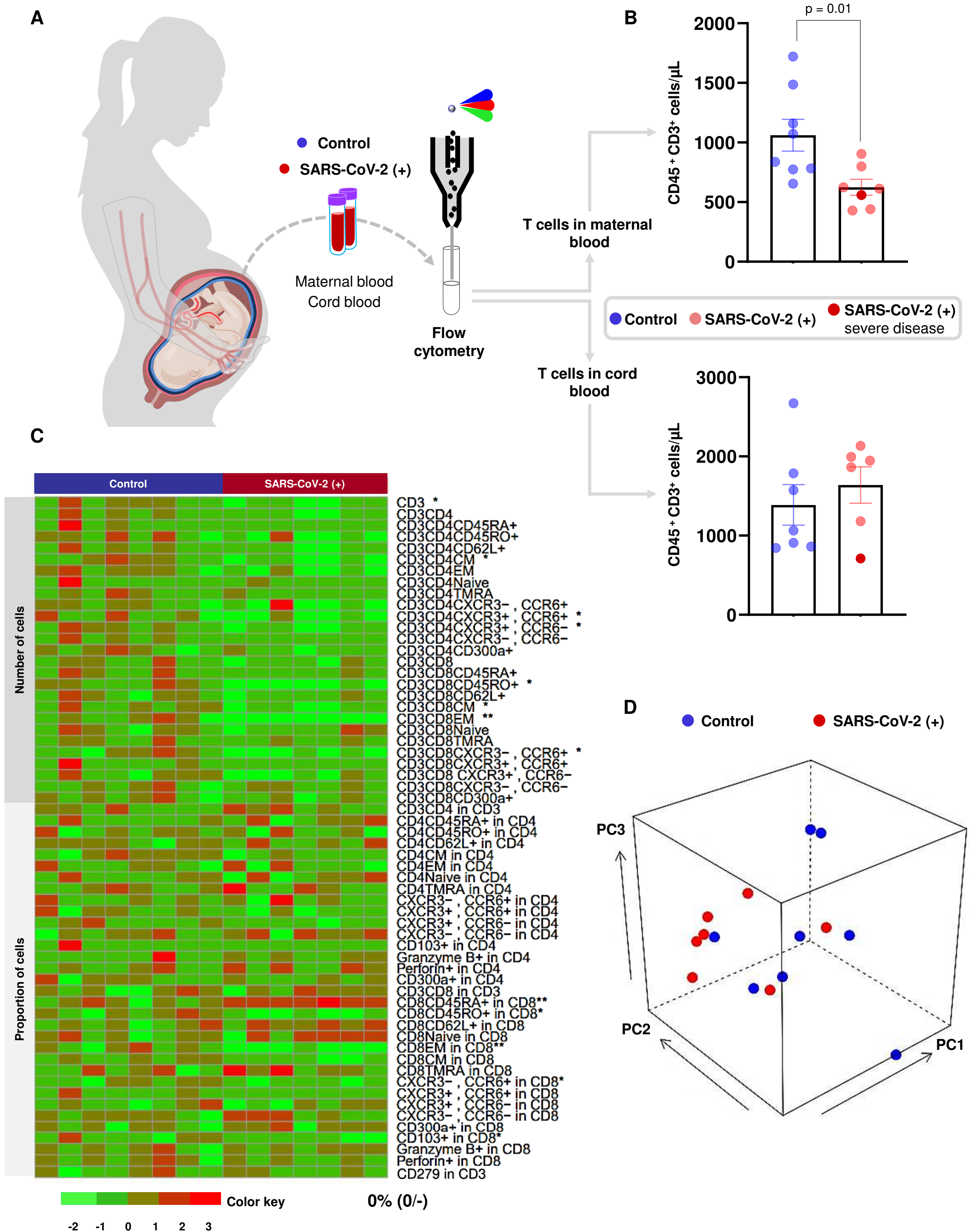


Figure 2. Immunophenotyping of T cells in pregnant women with SARS-CoV-2 infection and their neonates. (A) Maternal peripheral blood and cord blood were collected for immunophenotyping by flow cytometry. **(B)** Numbers of T cells in the maternal blood ($n = 7-8$ per group) and cord blood ($n = 6-7$ per group) from SARS-CoV-2 (+) or healthy pregnant women. Bar plots represent mean and standard error of the mean. Differences between groups were evaluated by Mann-Whitney U-tests. P values < 0.05 were used to denote a significant result. Blue dots indicate healthy pregnant women, light red dots indicate SARS-CoV-2 (+) pregnant women, and the dark red dot indicates one patient with severe COVID-19 disease. **(C)** Heatmap showing abundance (z-scores) for T cell subsets in the maternal blood from SARS-CoV-2 (+) or healthy pregnant women ($n = 7-8$ per group). Cell numbers and proportions are shown. Differences between groups were assessed using two-sample t-tests. P values were adjusted for multiple comparisons using false discovery rate (FDR) method to obtain q values. * $q < 0.1$; ** $q < 0.05$. Red and green indicate increased and decreased abundance, respectively. **(D)** Three-dimensional scatter plot showing the distribution of flow cytometry data from the maternal blood of SARS-CoV-2 (+) (red dots) or healthy pregnant women (blue dots) ($n = 7-8$ per group) based on principal component (PC)1, PC2, and PC3.

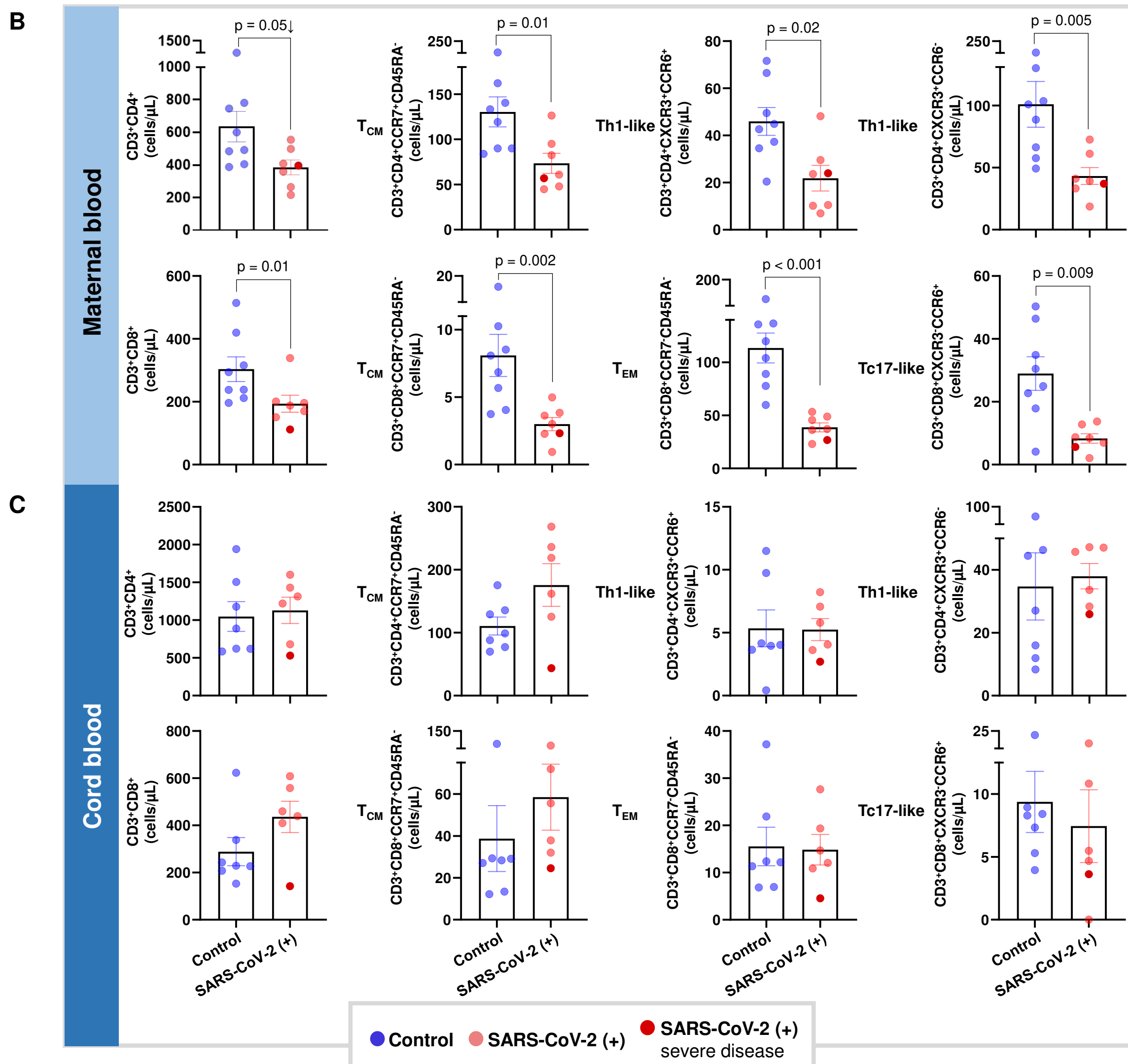
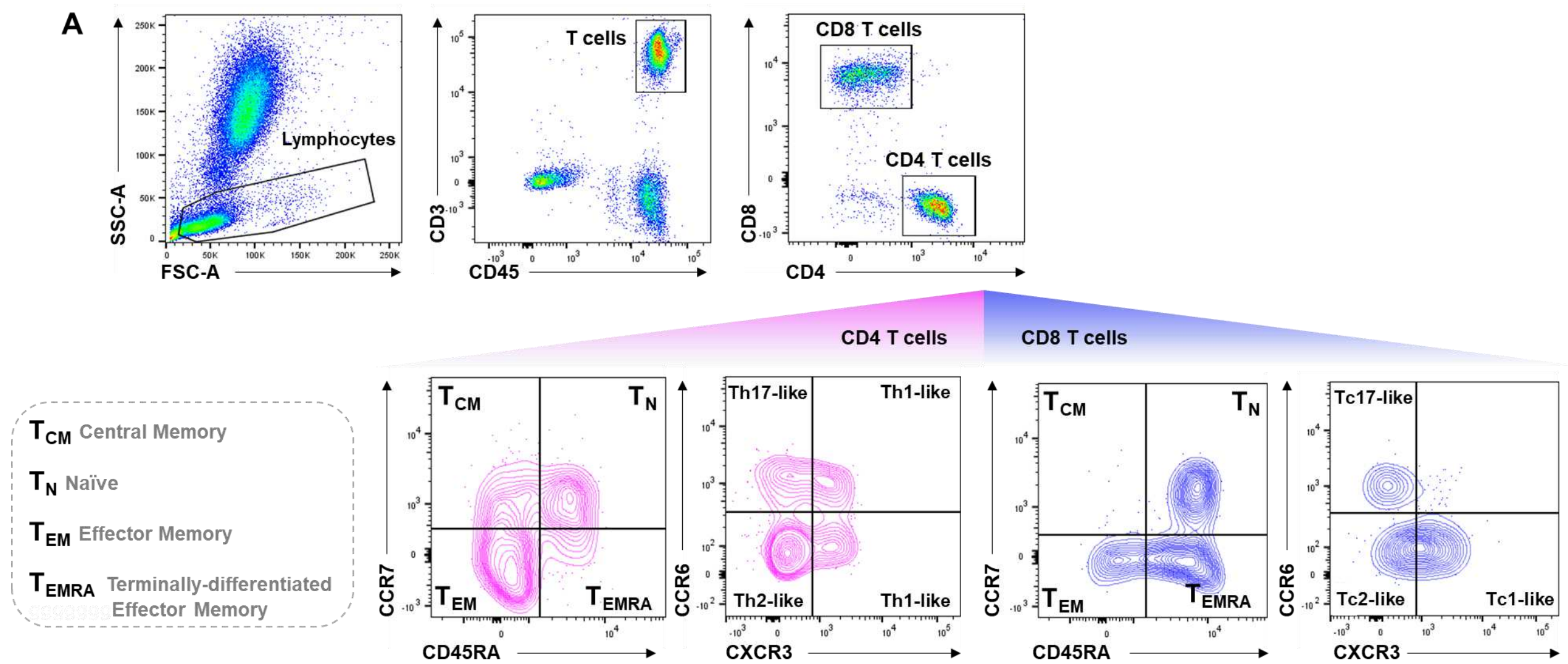


Figure 3. T cell subsets in pregnant women with SARS-CoV-2 infection and their neonates. (A) Representative gating strategy used to identify CD4⁺ and CD8⁺ T cells, and their respective subsets, within the total T cell population (CD45⁺CD3⁺ cells) in the maternal blood and cord blood. (B) Numbers of CD4⁺ T cells, CD4⁺ T_{CM}, CXCR3⁺CCR6⁺ Th1-like cells, and CXCR3⁺CCR6⁻ Th1-like cells (upper row); and the numbers of CD8⁺ T cells, CD8⁺ T_{CM}, CD8⁺ T_{EM}, and Tc17-like cells (lower row) in the maternal blood from SARS-CoV-2 (+) or healthy pregnant women (n = 7-8). (C) Numbers of CD4⁺ T cells, CD4⁺ T_{CM}, CXCR3⁺CCR6⁺ Th1-like cells, and CXCR3⁺CCR6⁻ Th1-like cells (upper row); and the numbers of CD8⁺ T cells, CD8⁺ T_{CM}, CD8⁺ T_{EM}, and Tc17-like cells (lower row) in the cord blood from SARS-CoV-2 (+) or healthy pregnant women (n = 6-7 per group). Bar plots represent mean and standard error of the mean. Differences between groups were evaluated by Mann-Whitney U-tests, with $p < 0.05$ being considered significant. Blue dots indicate healthy pregnant women, light red dots indicate SARS-CoV-2 (+) women, and the dark red dot indicates one patient with severe COVID-19 disease.

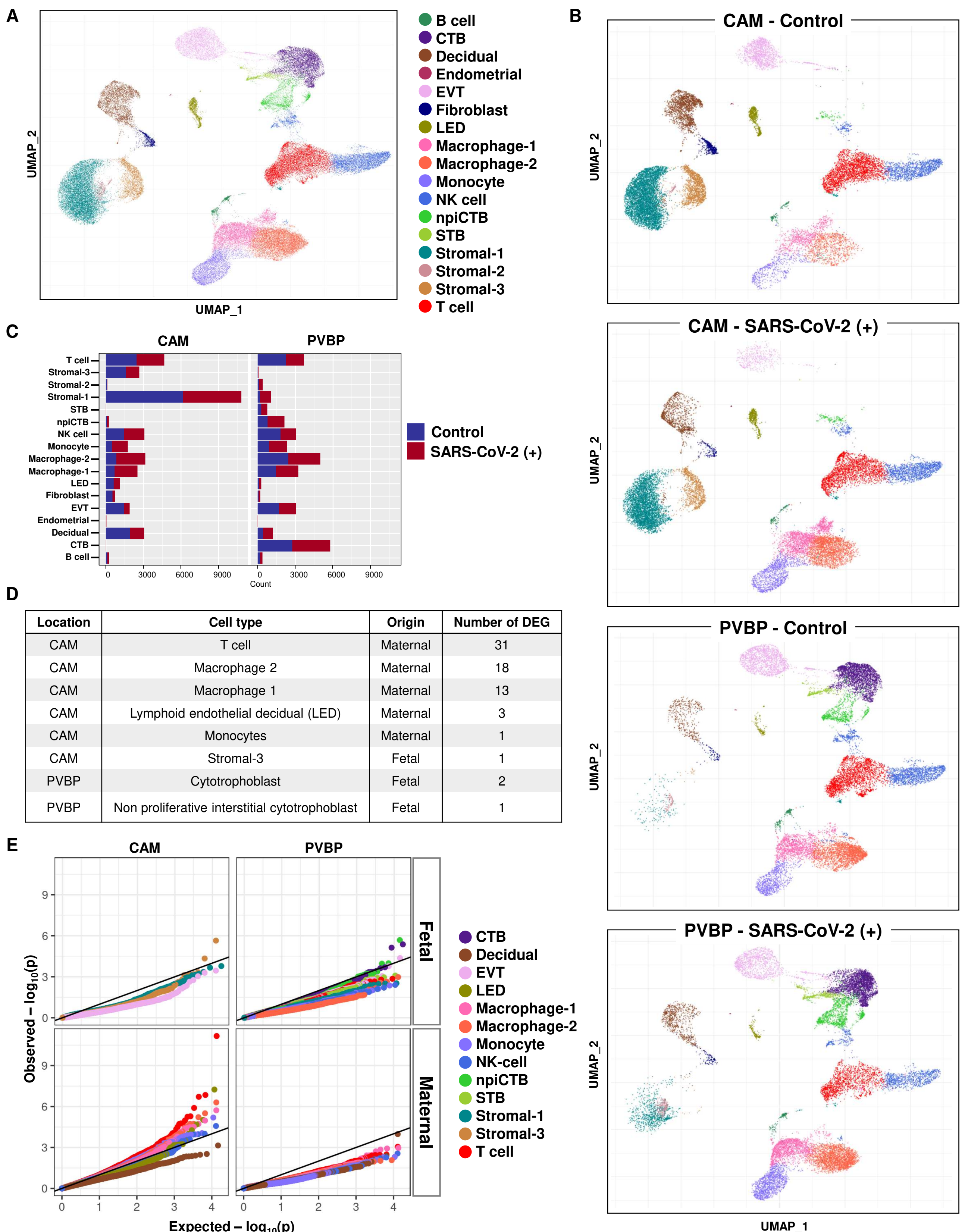


Figure 4. Single-cell RNA sequencing of the placental tissues of women with SARS-CoV-2 infection. (A) Uniform Manifold Approximation Plot (UMAP) showing the combined cell type classifications from the chorioamniotic membranes (CAM) and placental villi and basal plate (PVBP) of SARS-CoV-2 (+) or healthy pregnant women (n = 7-8 per group), where each dot represents a single cell. Abbreviations used are: CTB, cytotrophoblast; EVT, extravillous trophoblast; LED, lymphoid endothelial decidual cell; npICTB, non-proliferative interstitial cytotrophoblast; STB, syncytiotrophoblast. (B) UMAP showing cell populations separated based on placental compartment (CAM and PVBP) from SARS-CoV-2 (+) or healthy pregnant women. (C) Bar plot showing the numbers of cells of each type in the CAM and PVBP of SARS-CoV-2 (+) or healthy pregnant women. (D) Number of differentially expressed genes (DEG) in each cell type from the CAM and PVBP with false discovery rate (FDR) adjusted p < 0.1. (E) Quantile-quantile (Q-Q) plot showing differential expression of all tested genes in each cell type of maternal or fetal origin from the CAM and PVBP samples. Deviation above the 1:1 line (solid black line) indicates enrichment.

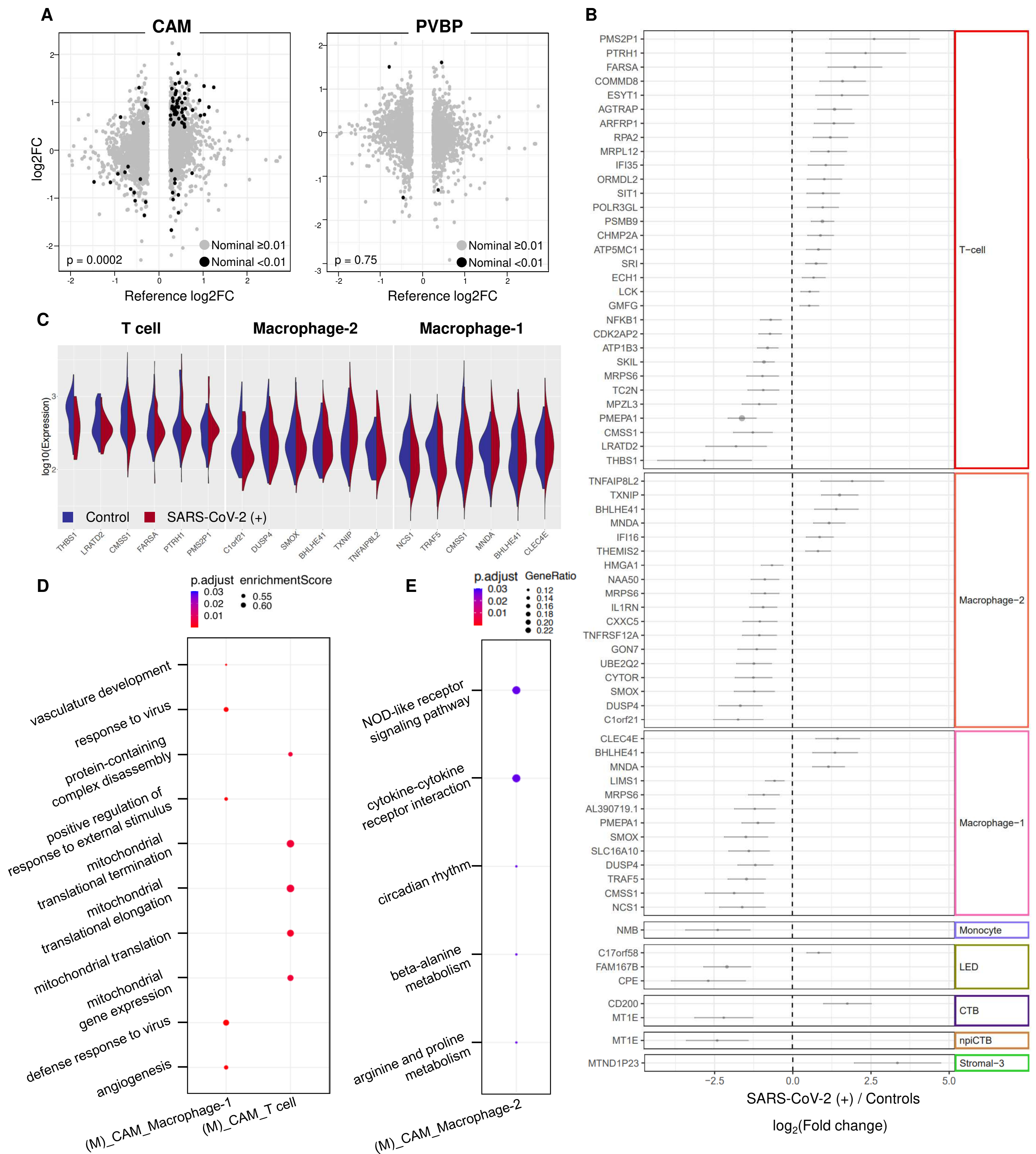


Figure 5. Single-cell characterization of T cells and macrophages from the chorioamniotic membranes (CAM) and placental villi and basal plate (PVBP). (A) Scatter plots showing the effects of SARS-CoV-2 on gene expression [\log_2 Fold Change (FC)] in T cells from the CAM and PVBP compared to a previously reported dataset (Meckiff et al., 2020). Black dots represent genes with nominal $p < 0.01$ in this study, which are used to calculate Spearman's correlation. (B) Forest plot showing differentially expressed genes in T cell, macrophage-2, macrophage-1, monocyte, lymphoid endothelial decidual cell (LED), cytotrophoblast (CTB), non-proliferative interstitial cytotrophoblast (npICTB), and stromal-3 cell populations in the CAM and PVBP of SARS-CoV-2 (+) or healthy pregnant women ($n = 7-8$ per group). Differentially expressed genes shown are significant after false discovery rate (FDR) adjustment ($q < 0.1$). (C) Violin plot showing the distribution of single-cell gene expression levels for the top three upregulated and downregulated genes in the maternal T cell, macrophage-1, and macrophage-2 populations in the CAM comparing between SARS-CoV-2 (+) and healthy pregnant women ($n = 7-8$ per group). (D) Gene ontology (GO) terms enriched in differentially expressed genes in the macrophage-1 and T cell populations of maternal (M) origin from CAM samples. GO terms with $q < 0.05$ are shown. (E) Kyoto Encyclopedia of Gene and Genomes (KEGG) pathways enriched for differentially expressed genes in macrophage-2 of maternal (M) origin from the CAM based on the over-representation analysis. KEGG pathways with $q < 0.05$ were selected.

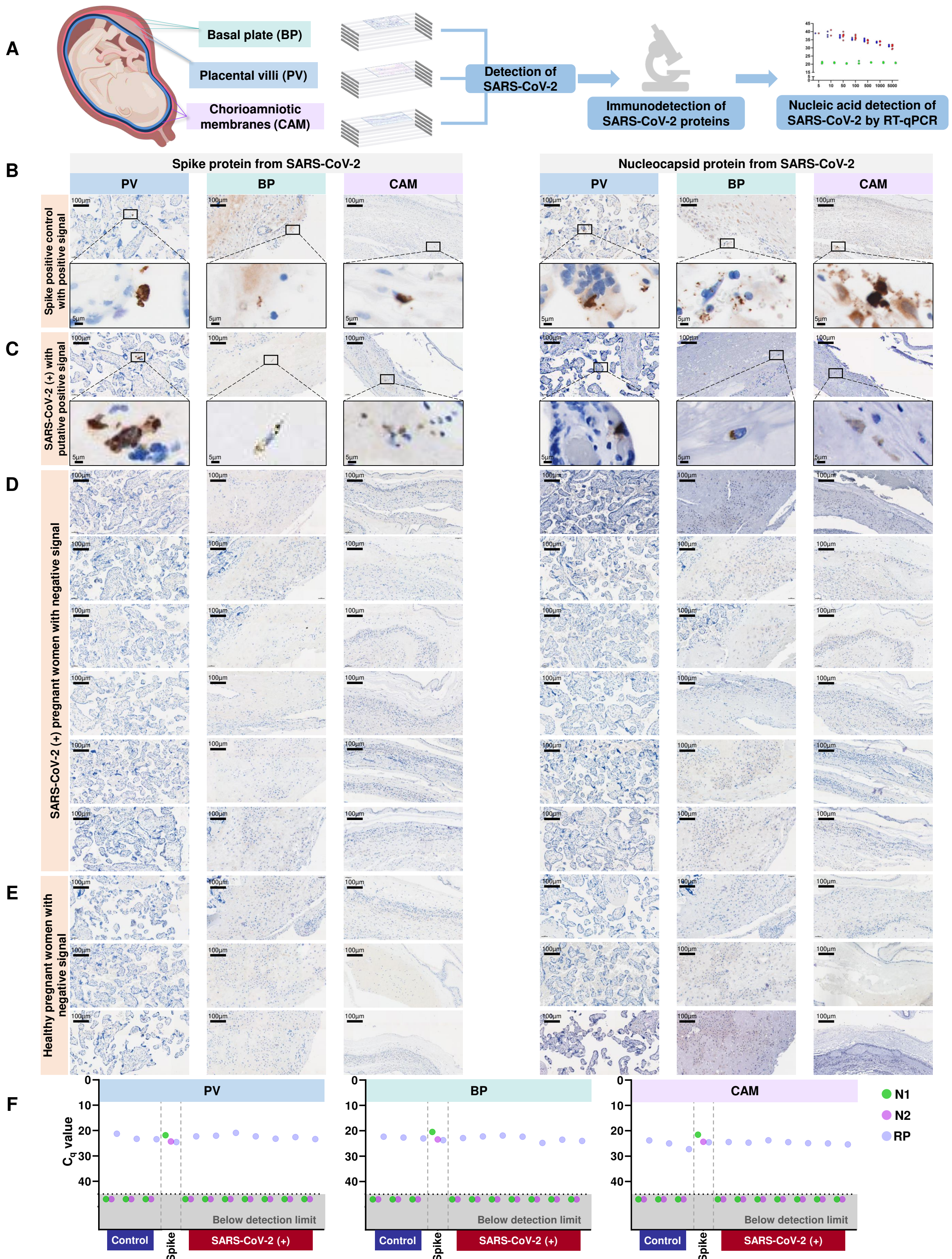


Figure 6. Immunohistological and molecular detection of SARS-CoV-2 proteins/RNA in the placenta of women with SARS-CoV-2 infection. (A) Schematic representation showing various sampling locations in the placental villi (PV), basal plate (BP), and chorioamniotic membranes (CAM) that were tested for SARS-CoV-2 proteins/RNA by immunohistochemistry and RT-qPCR, respectively. (B) Brightfield microscopy images showing positive signal for SARS-CoV-2 spike (left panel) and nucleocapsid (right panel) proteins in the PV, BP, and CAM of spike-in positive control. Brown color indicates putative positive staining. (C) Brightfield microscopy images showing putative positive signal for SARS-CoV-2 spike (left panel) and nucleocapsid (right panel) proteins in the PV, BP, and CAM of a SARS-CoV-2 (+) pregnant woman. (D) Brightfield microscopy images showing negative signal for SARS-CoV-2 spike (left panel) and nucleocapsid (right panel) proteins in the PV, BP, and CAM of SARS-CoV-2 (+) pregnant women. (E) Brightfield microscopy images showing negative signal for SARS-CoV-2 spike (left panel) and nucleocapsid (right panel) proteins in the PV, BP, and CAM of healthy pregnant women. (F) RT-qPCR results of SARS-CoV-2 viral RNA detection in the PV, BP, and CAM from formalin-fixed paraffin-embedded tissues from SARS-CoV-2 (+) and healthy pregnant women. N1 and N2 denote two SARS-CoV-2 nucleocapsid (N) genes, and RP denotes RNase P gene, which serves as a positive internal PCR control. Spike-in positive controls are also included. Undetermined quantification cycle (C_q) values are represented below the detection limit (gray area).

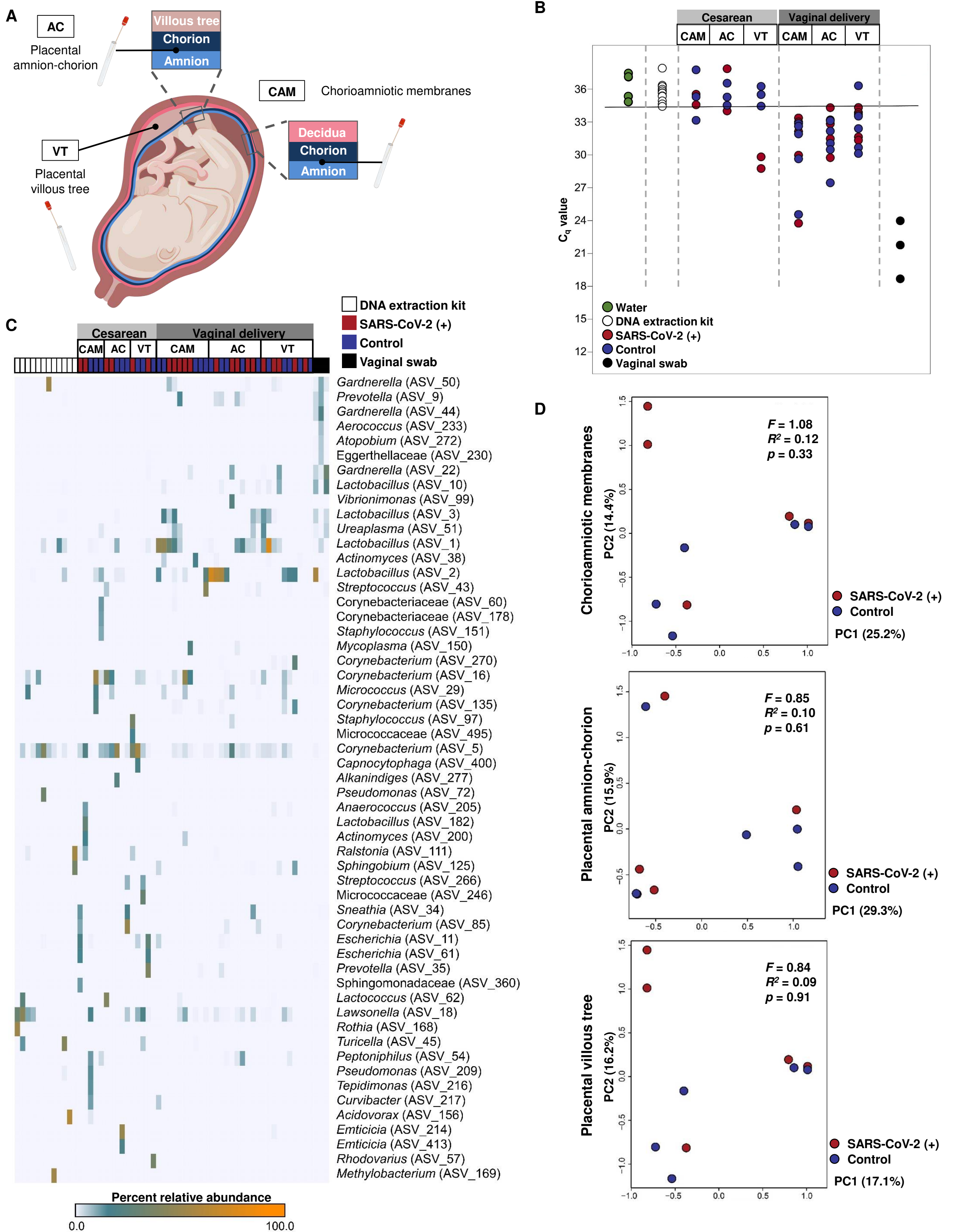


Figure 7. Bacterial DNA profiles of the placental tissues from pregnant women with SARS-CoV-2 infection. (A) Schematic representation of sampling locations from the chorioamniotic membranes (CAM), amnion-chorion interface of the placenta (AC), and within the placental villous tree (VT) from SARS-CoV-2 (+) pregnant women who delivered by cesarean section (n = 2) or vaginally (n = 5) and from healthy pregnant women who delivered by cesarean section (n = 3) or vaginally (n = 5). **(B)** Quantitative real-time PCR analyses illustrating the bacterial loads (i.e. 16S rDNA abundance) of the CAM, AC, and VT from SARS-CoV-2 (+) or healthy pregnant women (cesarean section or vaginal delivery). The solid black line denotes the lowest cycle of quantification (i.e. highest bacterial load) for any blank DNA extraction kit negative control. Data from three human vaginal swabs are included for perspective. **(C)** Heatmap illustrating the relative abundances of prominent (>2% average relative abundance) amplicon sequence variants (ASVs) among the 16S rRNA gene profiles of the CAM, AC, and VT from SARS-CoV-2 (+) or healthy pregnant women (cesarean section or vaginal delivery). Data from blank DNA extraction kit negative controls and human vaginal swabs are included for perspective. **(D)** Principal coordinates analyses (PCoA) illustrating similarity in the 16S rRNA gene profiles of the CAM, AC, and VT obtained through vaginal delivery from SARS-CoV-2 (+) or healthy pregnant women.

Figures

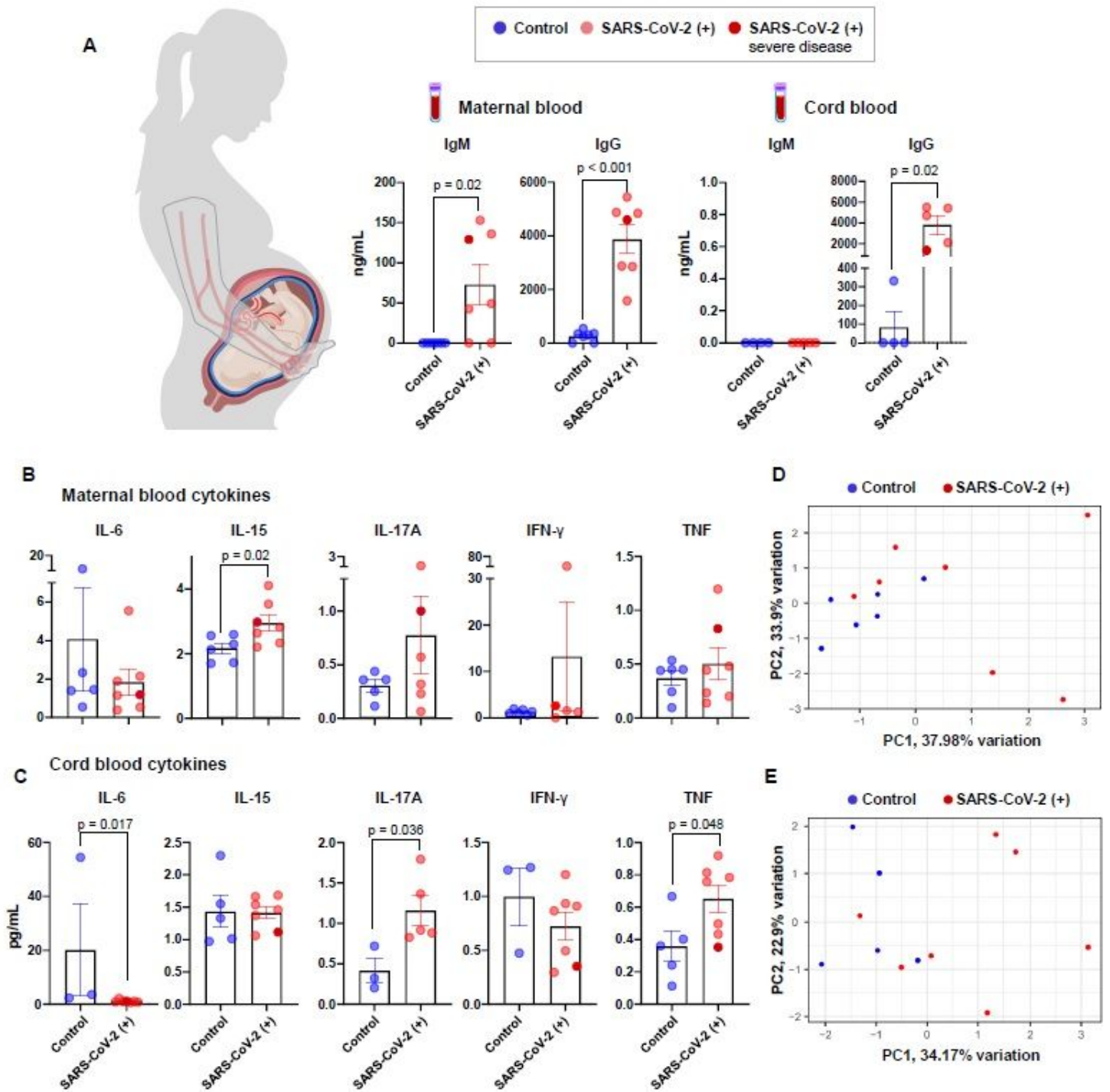


Figure 1

Serological and cytokine responses in pregnant women with SARS-CoV-2 infection and their neonates. (A) Serum concentrations of IgM and IgG in the maternal peripheral blood (n = 7 per group) (left panel) and cord blood (n = 4-5 per group) (right panel) from SARS-CoV-2 (+) or healthy pregnant women. Bar plots represent mean and standard error of the mean. Differences between two groups were evaluated by

Mann-Whitney U tests. (B) Plasma concentrations of IL-6, IL-15, IL-17A, IFN- γ , and TNF in the maternal peripheral blood (n = 6-7 per group). Blue dots indicate healthy pregnant women, light red dots indicate SARS-CoV-2 (+) pregnant women, and the dark red dot indicates one patient with severe COVID-19 disease. (C) Plasma concentrations of IL-6, IL-15, IL-17A, IFN- γ , and TNF in the cord blood (n = 5-7 per group). Blue dots indicate healthy pregnant women, light red dots indicate SARS-CoV-2 (+) pregnant women, and the dark red dot indicates one patient with severe COVID-19 disease. (D) Scatter plot of the first two principal components (PC1 and PC2) from cytokine concentrations in the maternal plasma. Blue dots indicate healthy pregnant women and red dots indicate SARS-CoV-2 (+) pregnant women. (E) Scatter plot of PC1 and PC2 from cytokine concentrations in the cord blood plasma. Blue dots indicate healthy pregnant women and red dots indicate SARS-CoV-2 (+) pregnant women. Bar plots represent mean and standard error of the mean. Differences in cytokine concentrations between groups were evaluated by Mann-Whitney U-tests. Differences in PC1 values between SARS-CoV-2 (+) and healthy pregnant women were assessed using two-sample student's t-tests. P values are considered significant when $p < 0.05$.

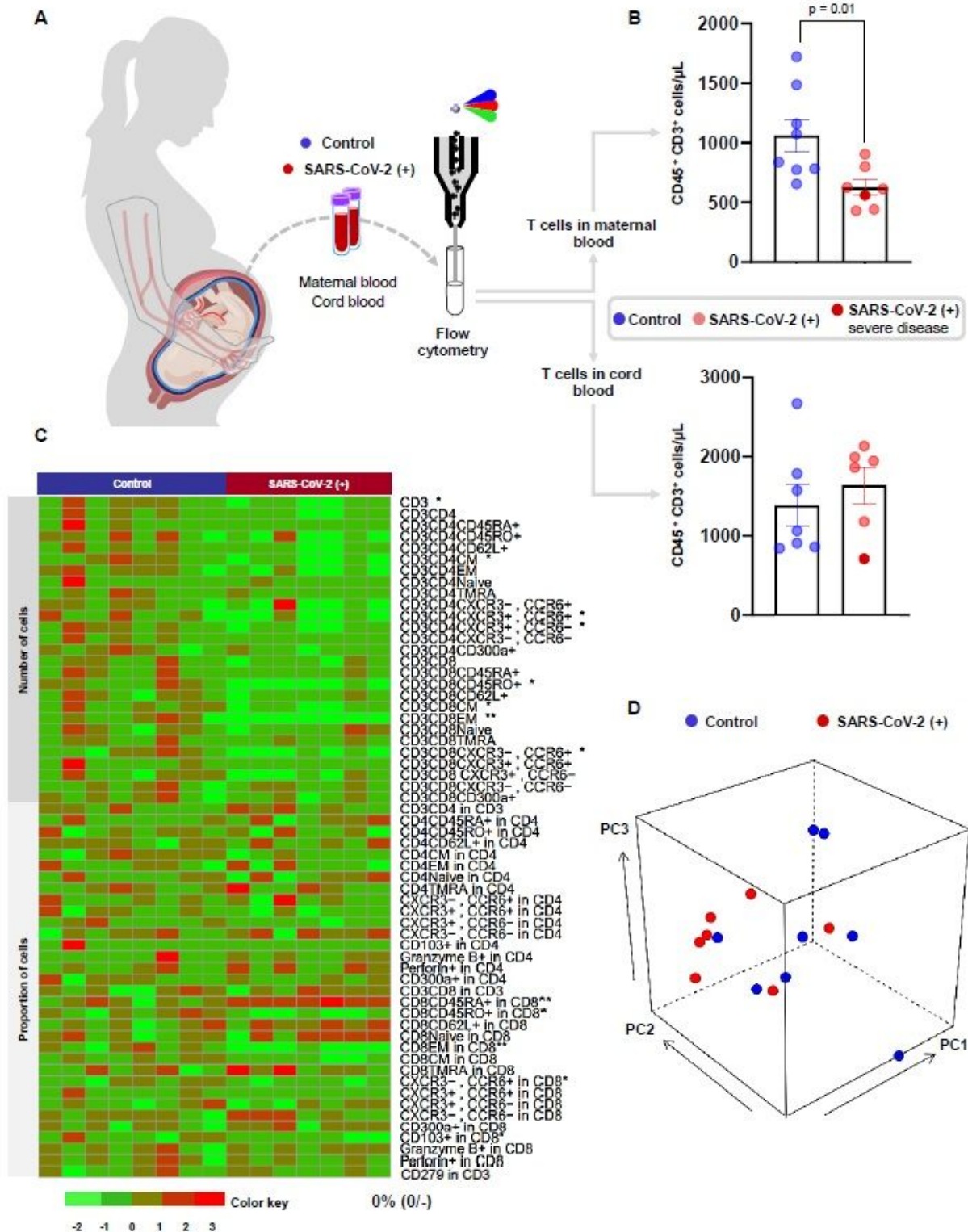


Figure 2

Immunophenotyping of T cells in pregnant women with SARS-CoV-2 infection and their neonates. (A) Maternal peripheral blood and cord blood were collected for immunophenotyping by flow cytometry. (B) Numbers of T cells in the maternal blood (n = 7-8 per group) and cord blood (n = 6-7 per group) from SARS-CoV-2 (+) or healthy pregnant women. Bar plots represent mean and standard error of the mean. Differences between groups were evaluated by Mann-Whitney U-tests. P values < 0.05 were used to

denote a significant result. Blue dots indicate healthy pregnant women, light red dots indicate SARS-CoV-2 (+) pregnant women, and the dark red dot indicates one patient with severe COVID-19 disease. (C) Heatmap showing abundance (z-scores) for T cell subsets in the maternal blood from SARS-CoV-2 (+) or healthy pregnant women (n = 7-8 per group). Cell numbers and proportions are shown. Differences between groups were assessed using two-sample t-tests. P values were adjusted for multiple comparisons using false discovery rate (FDR) method to obtain q values. * q < 0.1; ** q < 0.05. Red and green indicate increased and decreased abundance, respectively. (D) Three-dimensional scatter plot showing the distribution of flow cytometry data from the maternal blood of SARS-CoV-2 (+) (red dots) or healthy pregnant women (blue dots) (n = 7-8 per group) based on principal component (PC)1, PC2, and PC3.

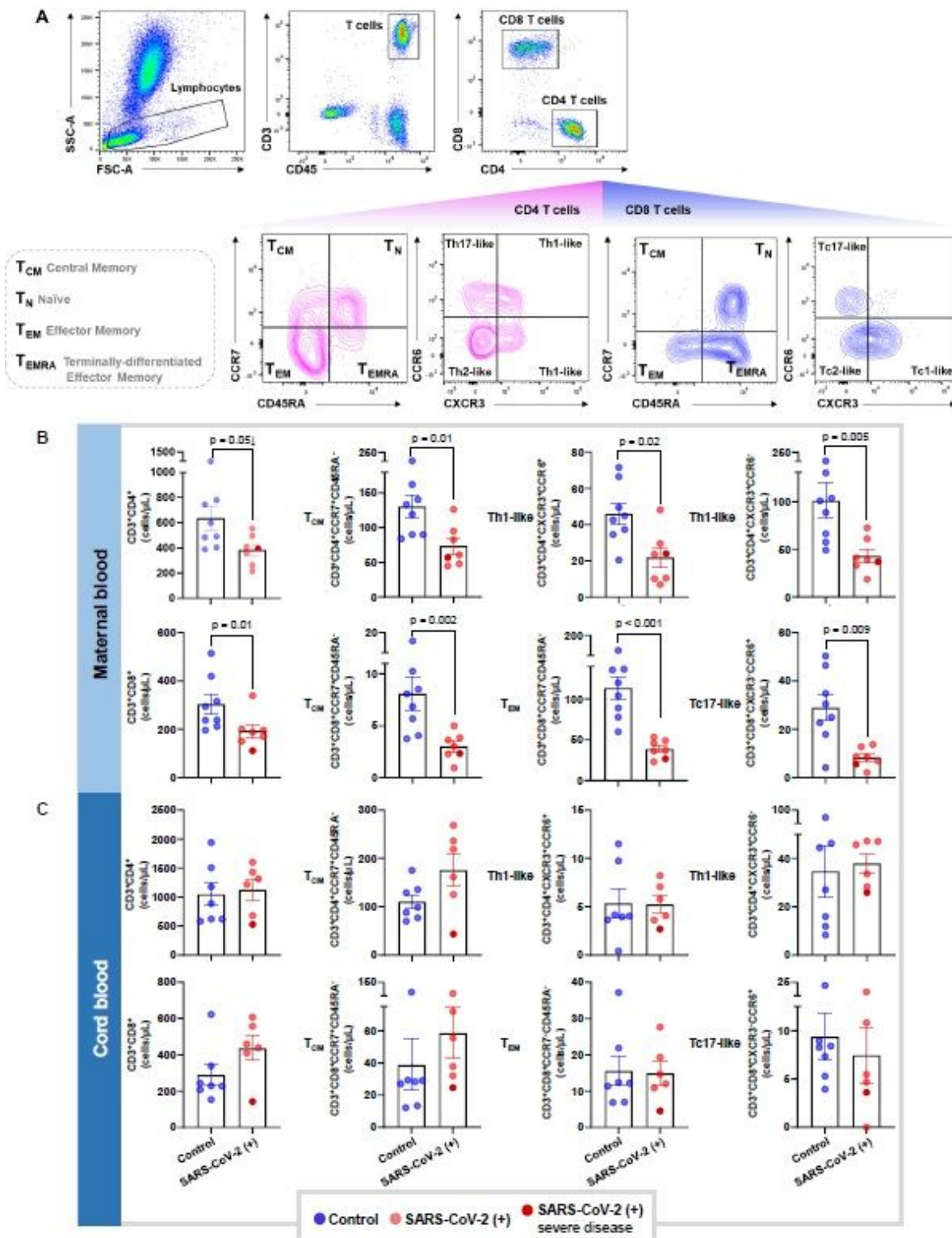


Figure 3

T cell subsets in pregnant women with SARS-CoV-2 infection and their neonates. (A) Representative gating strategy used to identify CD4⁺ and CD8⁺ T cells, and their respective subsets, within the total T cell population (CD45⁺CD3⁺ cells) in the maternal blood and cord blood. (B) Numbers of CD4⁺ T cells, CD4⁺ TCM, CXCR3⁺CCR6⁺ Th1-like cells, and CXCR3⁺CCR6⁻ Th1-like cells (upper row); and the numbers of CD8⁺ T cells, CD8⁺ TCM, CD8⁺ TEM, and Tc17-like cells (lower row) in the maternal blood from SARS-

CoV-2 (+) or healthy pregnant women (n = 7-8). (C) Numbers of CD4+ T cells, CD4+ TCM, CXCR3+CCR6+ Th1-like cells, and CXCR3+CCR6- Th1-like cells (upper row); and the numbers of CD8+ T cells, CD8+ TCM, CD8+ TEM, and Tc17-like cells (lower row) in the cord blood from SARS-CoV-2 (+) or healthy pregnant women (n = 6- 7 per group). Bar plots represent mean and standard error of the mean. Differences between groups were evaluated by Mann-Whitney U-tests, with p < 0.05 being considered significant. Blue dots indicate healthy pregnant women, light red dots indicate SARS-CoV-2 (+) women, and the dark red dot indicates one patient with severe COVID-19 disease.

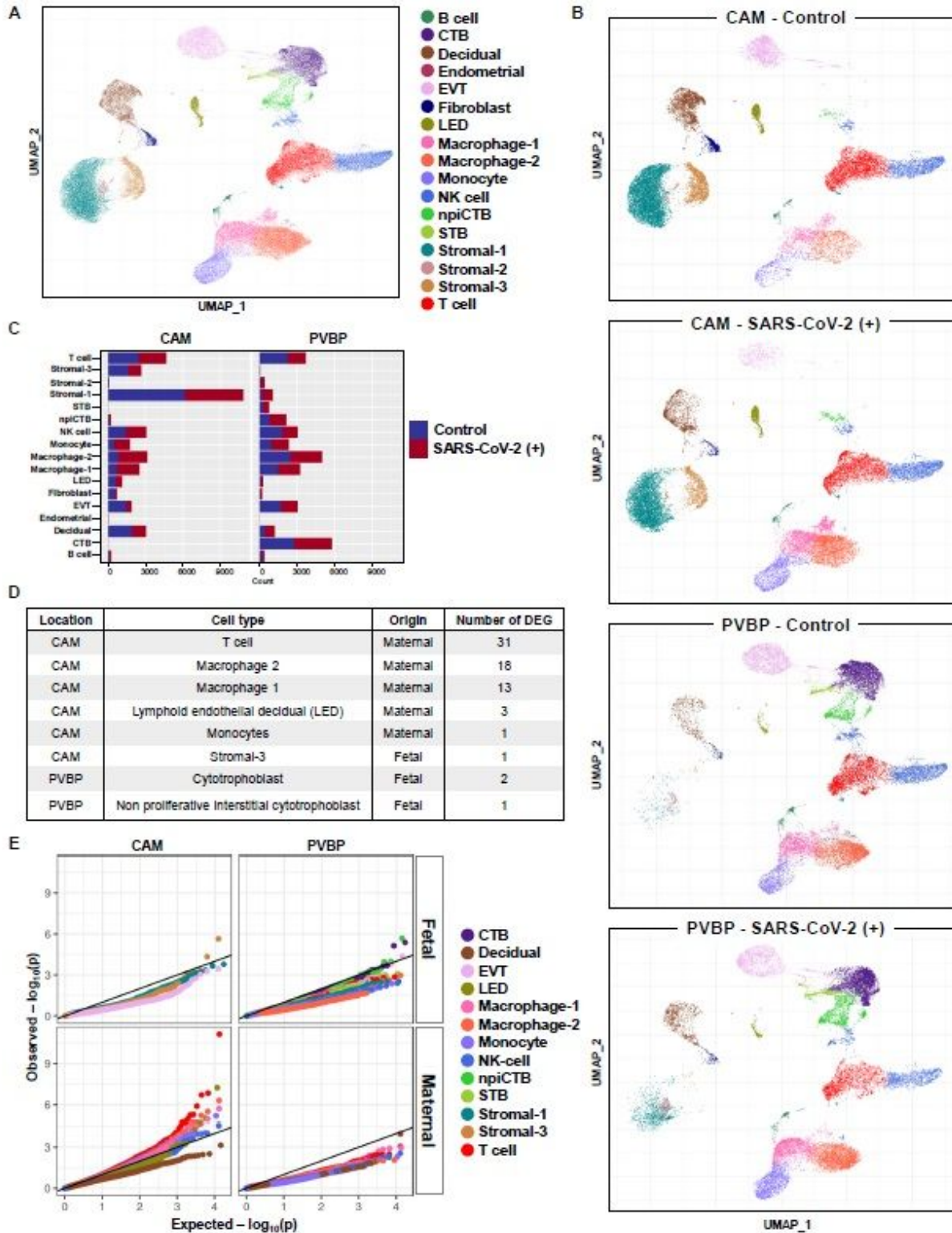


Figure 4

Single-cell RNA sequencing of the placental tissues of women with SARS-CoV-2 infection. (A) Uniform Manifold Approximation Plot (UMAP) showing the combined cell type classifications from the chorioamniotic membranes (CAM) and placental villi and basal plate (PVBP) of SARS-CoV-2 (+) or healthy pregnant women (n = 7-8 per group), where each dot represents a single cell. Abbreviations used are: CTB, cytotrophoblast; EVT, extravillous trophoblast; LED, lymphoid endothelial decidual cell; npICTB, non-proliferative interstitial cytotrophoblast; STB, syncytiotrophoblast. (B) UMAP showing cell populations separated based on placental compartment (CAM and PVBP) from SARS-CoV-2 (+) or healthy pregnant women. (C) Bar plot showing the numbers of cells of each type in the CAM and PVBP of SARS-CoV-2 (+) or healthy pregnant women. (D) Number of differentially expressed genes (DEG) in each cell type from the CAM and PVBP with false discovery rate (FDR) adjusted $p < 0.1$. (E) Quantile-quantile (Q-Q) plot showing differential expression of all tested genes in each cell type of maternal or fetal origin from the CAM and PVBP samples. Deviation above the 1:1 line (solid black line) indicates enrichment.

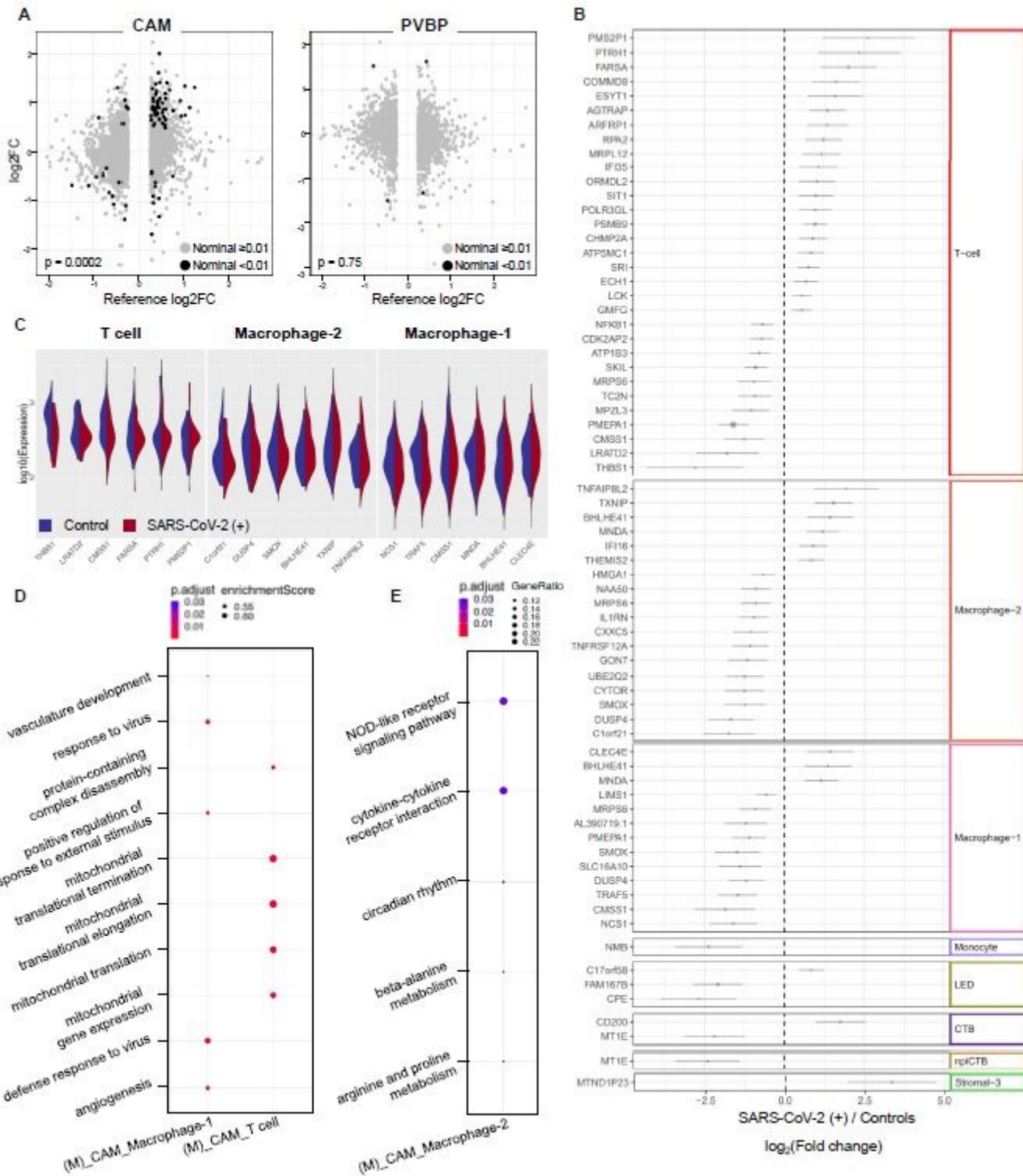


Figure 5

Single cell characterization of T cells and macrophages from the chorioamniotic membranes (and placental villi and basal plate (PVBP)..(Scatter plots showing the effects of SARS CoV 2 on gene expression [\log_2 Fold Change (in T cells from the CAM and PVBP compared to a previously reported dataset Meckiff et al 2020 Black dots represent genes with nominal $p < 0.01$ in this study, which are used to calculate Spearman's correlation ..(Forest plot showing differentially expressed genes in T cell,

macrophage 2 macrophage 1 monocyte, lymphoid endothelial decidual cell (cytotrophoblast (non proliferative interstitial cytotrophoblast npiCTB and stromal 3 cell populations in the CAM and PVBP of SARS CoV 2 or healthy pregnant women (n 7 8 per group) Differentially expressed genes shown are significant after false discovery rate (adjustment (q 0 1))..(Violin plot showing the distribution of single cell gene expression levels for the top three upregulated and downregulated genes in the maternal T cell, macrophage 1 and macrophage 2 populations in the CAM comparing between SARS CoV 2 and healthy pregnant women (n 7 8 per group)group)..(Gene ontology (terms enriched in differentially expressed genes in the macrophage 1 and T cell populations of maternal (origin from CAM samples GO terms with q 0 05 are shown ..(Kyoto Encyclopedia of Gene and Genomes (pathways enriched for differentially expressed genes in macrophage 2 of maternal (origin from the CAM based on the over representation analysis KEGG pathways with q 0 05 were selected

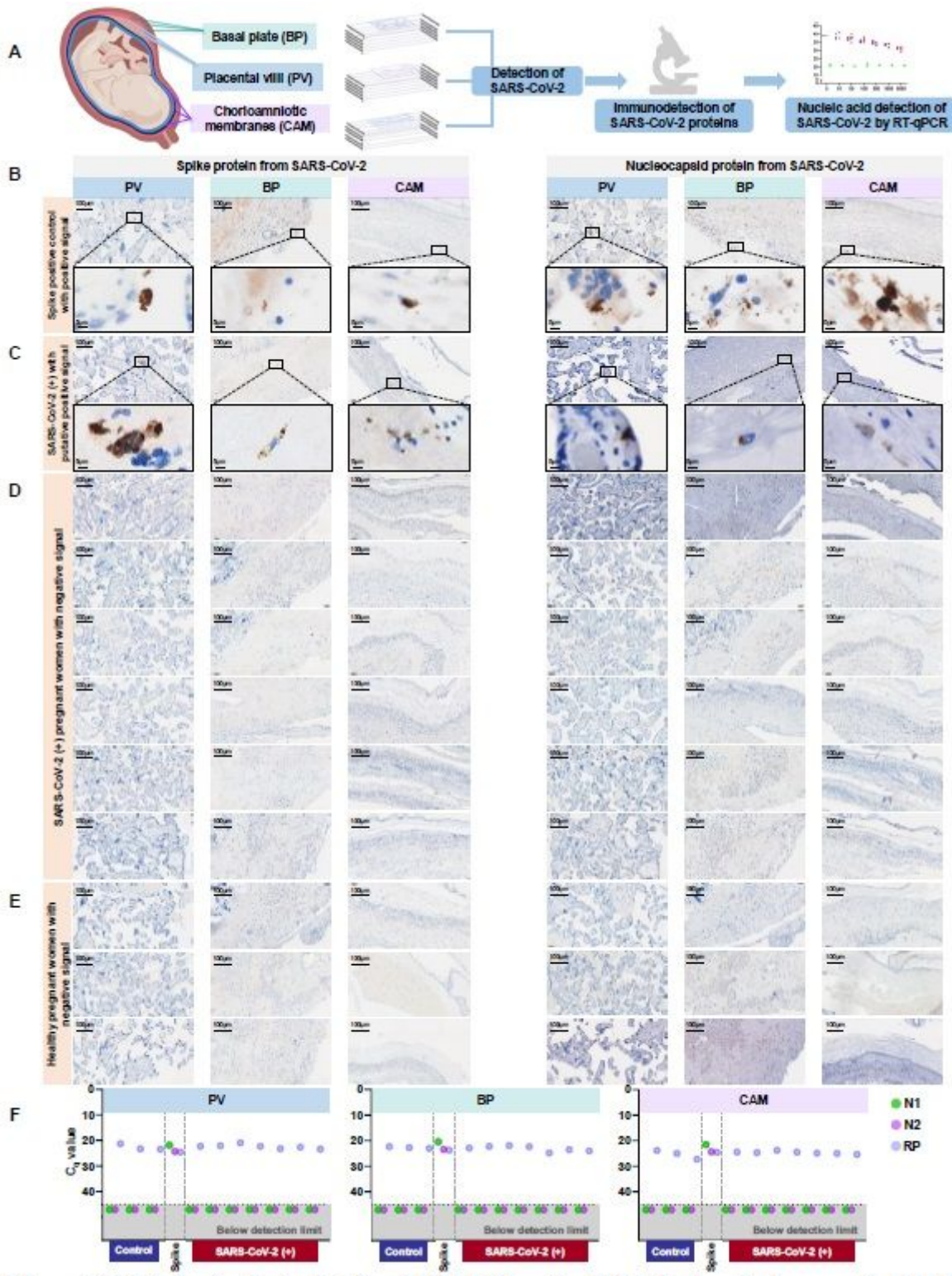


Figure 6

Immunohistological and molecular detection of SARS-CoV-2 proteins/RNA in the placenta of women with SARS-CoV-2 infection. (A) Schematic representation showing various sampling locations in the placental villi (PV), basal plate (BP), and chorioamniotic membranes (CAM) that were tested for SARS-CoV-2 proteins/RNA by immunohistochemistry and RT-qPCR, respectively. (B) Brightfield microscopy images showing positive signal for SARS-CoV-2 spike (left panel) and nucleocapsid (right panel) proteins in the

PV, BP, and CAM of spike-in positive control. Brown color indicates putative positive staining. (C) Brightfield microscopy images showing putative positive signal for SARS-CoV-2 spike (left panel) and nucleocapsid (right panel) proteins in the PV, BP, and CAM of a SARS-CoV-2 (+) pregnant woman. (D) Brightfield microscopy images showing negative signal for SARS-CoV-2 spike (left panel) and nucleocapsid (right panel) proteins in the PV, BP, and CAM of SARS-CoV-2 (+) pregnant women. (E) Brightfield microscopy images showing negative signal for SARS-CoV-2 spike (left panel) and nucleocapsid (right panel) proteins in the PV, BP, and CAM of healthy pregnant women. (F) RT-qPCR results of SARS-CoV-2 viral RNA detection in the PV, BP, and CAM from formalin-fixed paraffin-embedded tissues from SARS-CoV-2 (+) and healthy pregnant women. N1 and N2 denote two SARS-CoV-2 nucleocapsid (N) genes, and RP denotes RNase P gene, which serves as a positive internal PCR control. Spike-in positive controls are also included. Undetermined quantification cycle (Cq) values are represented below the detection limit (gray area). Figure

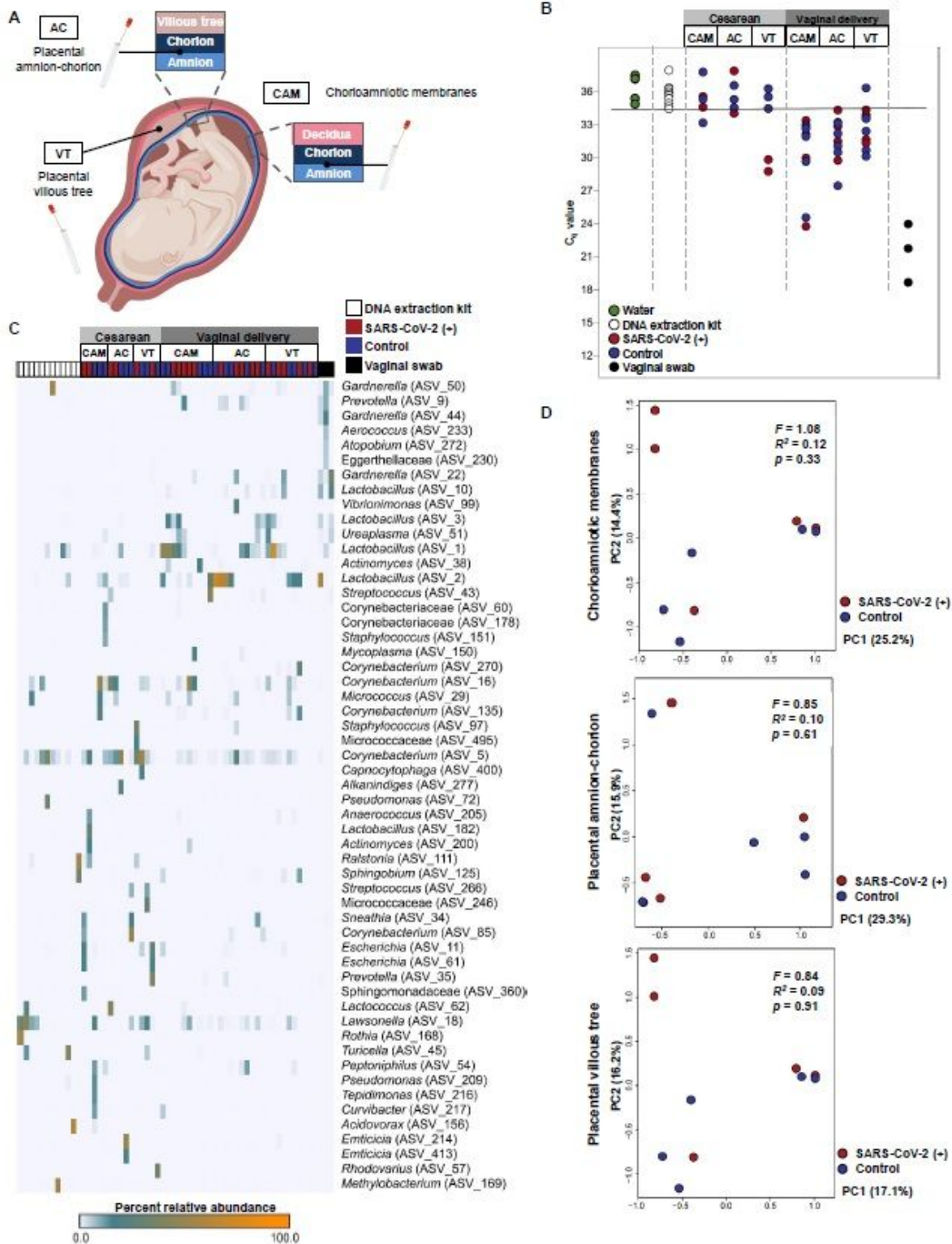


Figure 7

Bacterial DNA profiles of the placental tissues from pregnant women with SARS CoV 2 infection ..(Schematic representation of sampling locations from the chorioamniotic membranes (amnio chorion interface of the placenta (and within the placental villous tree (from SARS CoV 2 pregnant women who delivered by cesarean section (n 2 or vaginally (n 5 and from healthy pregnant women who delivered by cesarean section (n 3 or vaginally (n 5)..(Quantitative real time PCR analyses illustrating the bacterial

loads (i.e. 16 S rDNA abundance) of the CAM, AC, and VT from SARS CoV 2 or healthy pregnant women (cesarean section or vaginal delivery). The solid black line denotes the lowest cycle of quantification (i.e. highest bacterial load) for any blank DNA extraction kit negative control. Data from three human vaginal swabs are included for perspective. (Heatmap illustrating the relative abundances of prominent 2 average relative abundance) amplicon sequence variants (among the 16 S rRNA gene profiles of the CAM, AC, and VT from SARS CoV 2 or healthy pregnant women (cesarean section or vaginal delivery). Data from blank DNA extraction kit negative controls and human vaginal swabs are included for perspective. (Principal coordinates analyses PCoA illustrating similarity in the 16 S rRNA gene profiles of the CAM, AC, and VT obtained through vaginal delivery from SARS CoV 2 or healthy pregnant women

Supplementary Files

This is a list of supplementary files associated with this preprint. Click to download.

- [SupplementaryFiguresandTables.pdf](#)
- [SupplementaryTable3.xlsx](#)